https://doi.org/10.5194/essd-2021-170
Preprint. Discussion started: 25 May 2021

Open Access Earth System Science Data Discussions

Sea surface height anomaly and geostrophic velocity from altimetry measurements over the Arctic Ocean (2011-2018)

Francesca Doglioni[1], Robert Ricker[1], Benjamin Rabe[1], and Torsten Kanzow[1,2]

[1]Alfred Wegener Institute, Helmholtz Centre for Polar and Marine Research, Bremerhaven, Germany.
[2]Department 1 of Physics and Electrical Engeneering, Universität Bremen, Germany.

Correspondence: Francesca Doglioni (francesca.doglioni@awi.de)

Abstract.

In recent decades the decline of the Arctic sea ice has modified vertical momentum fluxes from the atmosphere to the ice and the ocean, thereby affecting the surface circulation. In the past ten years satellite altimetry has contributed to understand these changes. However, data from ice-covered regions require dedicated processing, originating inconsistency between ice-covered and open ocean regions in terms of biases, corrections and data coverage. Thus, efforts to generate consistent Arctic-wide datasets are still required to enable the study of the Arctic Ocean surface circulation at basin-wide scales. Here we provide and assess a monthly gridded dataset of sea surface height anomaly and geostrophic velocity. This dataset is based on Cryosat-2 observations over ice-covered and open ocean areas of the Arctic up to 88º N for the period 2011 to 2018, interpolated using the Data-Interpolating Variational Analysis (DIVA) method. Geostrophic velocity was not available north of 82° N before this study. To examine the robustness of our results, we compare the generated fields to one independent altimetry dataset and independent data of ocean bottom pressure, steric height and near-surface ocean velocity from moorings. Results from the comparison to near-surface ocean velocity show that our geostrophic velocity fields can resolve seasonal to interannual variability of boundary currents wider than about 50 km. We further discuss the seasonal cycle of sea surface height and geostrophic velocity in the context of previous literature. Large scale features emerge, i.e. Arctic-wide maximum sea surface height between October and January, with the highest amplitude over the shelves, and basin wide seasonal acceleration of Arctic slope currents in winter. We suggest that this dataset can be used to study not only the large scale sea surface height and circulation but also the regionally confined boundary currents. The dataset is available in netCDF format from PANGAEA at [data currently under review].

1 Introduction

The sea ice decline due to atmospheric warming in the Arctic Ocean has resulted in the modification of vertical momentum fluxes from the atmosphere to the ice and the ocean. Evidence of a positive trend, particularly strong in the summer season, has been found in sea ice drift observations (Spreen et al., 2011; Kwok et al., 2013; Kaur et al., 2018). Likewise, strong intensification of the surface ocean circulation has been documented in large scale circulation systems such as the Beaufort Gyre and the Transpolar Drift (McPhee, 2012; Armitage et al., 2016; Ma et al., 2017). However, it is currently not well known

https://doi.org/10.5194/essd-2021-170
Preprint. Discussion started: 25 May 2021

how near-surface ocean currents diverge from the ice drift, since the presence of ice limits the amount of direct observations of the upper ocean.

Before the advent of satellite observations, the large scale Arctic Ocean surface circulation was partially reconstructed from in-situ data and models, albeit with limitations in terms of spatial extent or processes represented. On the one hand, in-situ observations of surface ocean currents are sparse due to the remoteness of the Arctic environment and to the high risk of loosing sensors in ice-covered areas (Haller et al., 2014). On the other hand, while numerical models allow for the study of basin-wide processes, they rely largely on theoretical formulation of physical processes, often constrained by insufficient in-situ observations (Proshutinsky and Johnson, 1997; Jahn et al., 2010). Satellite-derived data then provided novel alternatives to tackle these issues. For instance, based on assumptions of the ice response to wind forcing (i.e., free drift), Kwok et al. (2013) used satellite sea ice drift observations to deduce near-surface ocean circulation.

Beyond ice drift observations, satellite altimetry can provide a more direct way to observe near-surface ocean currents. This is because altimetry derived sea surface height can be used to compute the geostrophic velocity, a component of the ocean surface velocity which is dominant in the Arctic on spatial scales larger than ten kilometres (Nurser and Bacon, 2014) and time scales longer than a few days. Satellite altimetry missions over the Arctic Ocean started twenty years ago, with the first missions covering it only partially in space and time (e.g., ERS 1 and 2, Envisat, CryoSat-2, ICEsat-1 and -2, Sentinel-3), but with coverage up to 88° N being provided by the CryoSat-2 mission since 2010 (Wingham et al., 2006).

Methodological developments of altimetry were originally aimed at the study of the cryosphere (Laxon, 1994; Alexandrov et al., 2010; Ricker et al., 2014; Armitage and Davidson, 2014), with efforts towards the generation of altimetric datasets for oceanographic purposes being made later (e.g., Bouffard et al., 2017). Initially, oceanographic datasets were limited either to the open ocean or to the ice-covered ocean (Kwok and Morison, 2011, 2016; Mizobata et al., 2016). Only in the last five years have few basin-wide multi-annual gridded sea surface height datasets been generated (Armitage et al., 2016; Rose et al., 2019; Guillot and Prandi, 2020).

There are some caveats though. It is not known how these products compare to each other, nor to what extent are their spatial and temporal resolution robust (e.g., noise to signal ratio). Differences between these datasets might be introduced by the altimeter signal processing (Ricker et al., 2014; Armitage and Davidson, 2014; Passaro et al., 2014), measurements corrections (Carrère et al., 2016; Ricker et al., 2016; Birol et al., 2017) and/or interpolation of observations onto regular grids. Yet, to date there have been only few assessments of altimetry-derived sea surface height and circulation relative to in situ data. These have focused on few areas such as the Nordic seas, the Barents Sea, the Beaufort Gyre and coasts. Assessments for other regions where currents play an important role for the global climate, such as the Arctic gateways and the Arctic continental slopes, remain to be done.

In this study we provide a new Arctic-wide gridded dataset of sea surface height and geostrophic velocity at monthly resolution over the period 2011 to 2018. This dataset was obtained from Cryosat-2 observations covering both the ice-covered and ice-free Arctic Ocean. Our specific objectives are:

- to document the methods used to produce the monthly sea surface height and geostrophic velocity fields;

https://doi.org/10.5194/essd-2021-170
Preprint. Discussion started: 25 May 2021

Open Access Earth System Science Data Discussions

– to indicate methodological steps likely to introduce noise or biases in altimetry gridded products at monthly resolution, via a comparison with an independent altimetry dataset;

– to assess this dataset through comparisons with in situ data from the Fram Strait and the Laptev Sea continental slope, and to provide indications regarding its temporal and spatial resolution.

This paper is structured as follows. In Sect. 2 we describe how altimetry-derived variables are commonly calculated, thereby defining the notation used in this work. In Sect. 3 we provide a description (e.g, sources, spatial and temporal coverage) of: the altimetry data used to derive our monthly dataset; the independent altimetry and moorings datasets used for evaluation; and the model data used to determine the appropriate length scales for the interpolation of altimetry. In the methods section we first describe the in-situ data processing (Sect. 4.1) and then the derivation of monthly gridded sea surface height and geostrophic velocity from altimetry observations (Sect. 4.2, 4.3, 4.4). In Sect. 5 we present the monthly fields and their evaluation against independent altimetry measurements and in-situ data. Comparing against in-situ data we identify the temporal and spatial scales over which they have highest agreement. In the same section we also describe the seasonal cycle emerging from the final monthly maps. Lastly, in Sect. 6 we discuss the spatial and temporal resolution of our dataset and put its seasonal cycle in context with other studies.

2 Ocean altimetry background

Relevant to physical oceanography are the steric and mass changes affecting the vertical extent of the ocean water column. The sum of these two components, known as dynamic ocean topography (η), can be derived from measurements of sea surface height (h), as obtained from satellite altimetry. h is the ocean height over a reference ellipsoid (WGS84 for Cryosat-2) and is calculated by subtracting the measurement of the satellite range to the sea surface (R) from the satellite altitude H over the ellipsoid (Eq. 1):

$$h = H - (R + C) \tag{1}$$

where C are corrections to the R measurement. η is then derived from h by removing the geoid height (G), i.e. the static ocean height component given the Earth's gravitational field, as follows (Eq. 2):

$$\eta(t) = h(t) - G \tag{2}$$

We use in this work along track datasets of sea surface height anomaly η', the time varying component of η. This is given by h referenced to a long-term mean sea surface height $\langle h \rangle$ (Eq. 3):

$$\eta'(t) = h'(t) = h(t) - \langle h \rangle \tag{3}$$

In order to compute the absolute geostrophic velocity, we reconstruct the full η by adding the mean dynamic topography $\langle \eta \rangle$, the temporal mean of η. This is derived from $\langle h \rangle$ by removing G, as estimated via a geoid model (e.g., Rio et al., 2011; Farrell et al., 2012; Knudsen et al., 2019; Mulet et al., 2021).

https://doi.org/10.5194/essd-2021-170
Preprint. Discussion started: 25 May 2021


Open Access Earth System Science Data Discussions

η is used to derive geostrophic velocities at the sea surface. Geostrophic velocities result from the balance of the pressure gradient force and the Coriolis force (Eq. 4):

$$\begin{cases} u_g = -\frac{g}{f}\frac{\partial \eta}{\partial y} \\ v_g = \frac{g}{f}\frac{\partial \eta}{\partial x} \end{cases} \quad (4)$$

where g is the gravitational acceleration and f is the Coriolis parameter.

The nomenclature introduced in this section will be used below to describe the datasets used and the ones resulting from the present analysis.

3 Data

3.1 Cryosat-2 sea surface height in ice-covered and ice-free regions

The monthly gridded dataset generated in this study is based on two sets of η' observations, one over ice-covered and a second over ice-free areas. Observations are from the European Space Agency's (ESA) Cryosat-2 mission, provided along the satellite tracks (ESA level L2, Bouzinac (2012)). For ice-covered areas we use the Alfred Wegener Institute (AWI) dataset data version 2.2 (Hendricks and Ricker, 2019); year round (including summer), with along-track resolution of 300 m. In this dataset, radar echoes from the surface are classified into sea ice and open water. Then, sea surface elevations from openings in the sea ice cover (i.e. leads) are retrieved using a retracking algorithm (Ricker et al., 2014). The processing includes waveforms in the Synthetic Aperture Radar (SAR) and the interferometric SAR (SARIn) modes (ESA level L1b dataset; see the areas covered by each altimeter mode at http://cryosat.mssl.ucl.ac.uk/qa/mode.php). Over the open ocean we use observations archived in the Radar Altimetry Database System, with along-track resolution of 7 km (RADS, Scharroo et al. (2013)).

From both datasets we select observations between 60º N and 88º N over the period 2011-2018. A caveat is however, that neither of these two datasets includes observations in the marginal ice zone (ice concentration between 15% and 70%), given that neither the AWI nor the RADS retracking models can fit both of open ocean and leads waveforms. Therefore, we acknowledge a data gap between 15% and 70% ice concentration.

All η' observations are referenced to the global DTU15MSS mean sea surface (Technical University of Denmark, updated from the DTU13MSS described in Andersen et al. (2015)), which uses multimission altimeter data including the satellites Envisat, ICEsat and Cryosat-2. To reconstruct η, we added our final gridded η' to the mean dynamic topography DTU17MDT, which is the DTU15MSS relative to the OGMOC geoid model (Knudsen et al., 2019).

3.2 Datasets used for comparisons

We use independent satellite and in-situ datasets to evaluate the final altimetry-derived η' and (u_g, v_g) monthly fields. Furthermore, model data are used to determine the decorrelation length scale used for the interpolation. These datasets are described below and their location is indicated in Fig.1.

https://doi.org/10.5194/essd-2021-170
Preprint. Discussion started: 25 May 2021

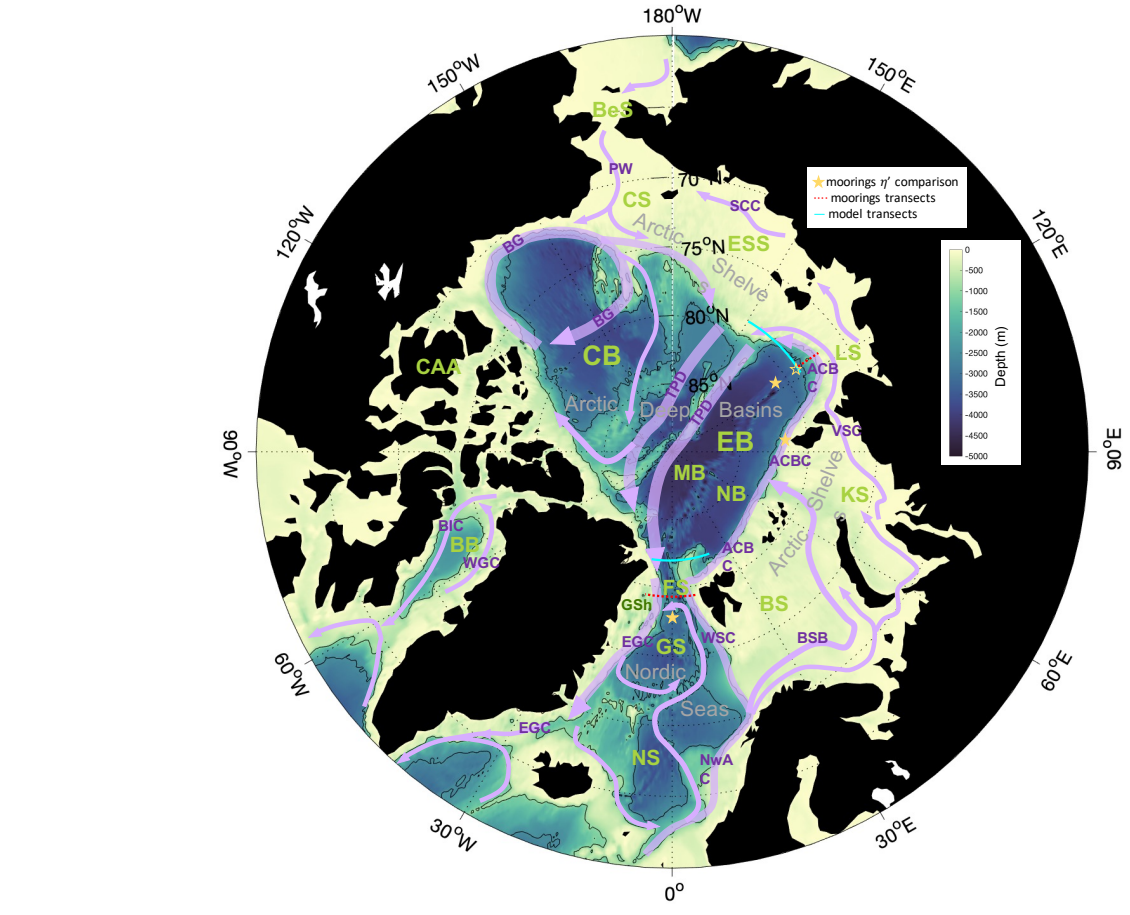

Figure 1. Arctic Ocean map and bathymetry (IBCAO) with the main sub-regions (green acronyms) and the mean surface circulation pathways (purple arrows and acronyms). Depth contours are drawn at 1000 m and 2000 m depth. **Regions**: Nordic Seas: Greenland Sea (GS), Norwegian Sea (NS); Arctic Shelves: Barents Sea (BS), Kara Sea (KS), Laptev Sea (LS), Eastern Siberian Shelf (ESS), Chukchi Sea (CS), Greenland Shelf (GSh); Arctic Deep Basins: Canada Basin (CB), Eurasian Basins (EB) (Nansen Basin (NB)); Baffin Bay (BB); Canadian Arctic Archipelago (CAA); Fram Strait (FS); Bering Strait (BeS). **Currents**: West Spitsbergen Current (WSC); Norwegian Atlantic Current (NwAC); Barents Sea Branch (BSB); Vilkitsky Strait Current (VSC); Arctic Circumpolar Boundary Current (ACBC); Siberian Coastal Current (SCC); Pacific Water inflow (PW); Beaufort Gyre (BG); TransPolar Drift (TPD); East Greenland Current (EGC); West Greenland Current (WGC); Baffin Island Current (BIC).

https://doi.org/10.5194/essd-2021-170
Preprint. Discussion started: 25 May 2021

3.2.1 Sea surface height

Monthly η' fields were compared to an independent satellite gridded dataset over the entire Arctic. This dataset is described by Armitage et al. (2016) and will be hereafter referret to as CPOM DOT (Centre for Polar Observation and Modelling Dynamic Ocean Topography, available at http://www.cpom.ucl.ac.uk/dynamic_topography). The CPOM DOT is a regional Arctic dataset spanning the years 2003-2014, derived from sea surface height observations (relying on the Envisat and Cryosat-2 satellite missions) and a geoid model (GOCO3s). Monthly fields are provided on a $0.75° \times 0.25°$ longitude-latitude grid, up to a latitude of 82° N.

We also compared η' locally, to the sum of in-situ measurements of steric height (the height component due to changes in density) and bottom pressure equivalent height (related to changes in water mass). These two components were derived from temperature, salinity and ocean bottom pressure data from moorings at three sites. The moorings were located in the southern Fram Strait ([78.17º N, 0º E], hereafter FS_S), at the shelf break north of Arctic Cape, the headland of Severnaya Zemlya ([82.22º N, 94.85º E], hereafter AC), and down the continental slope north of the Laptev Sea ([78.46º-81.15º N, 125.70º E], moorings M1_4 and M1_6). FS_S is part of a meridional mooring array deployed by the Alfred Wegener Institute (AWI) in the Fram Strait between 2016 and 2018. This mooring was composed of three Conductivity-Temperature-Depth (CTD) sensors at depths of 49 m, 231 m, and 729 m. Data are available through PANGAEA (von Appen et al., 2019). The AC is one of seven moorings deployed between 2015 and 2018 within the context of the German-Russian project Changing Arctic Transpolar System (CATS). This mooring was composed of six CTD sensors at 50 m, 131 m, 196 m, 293 m, 593 m, and 1448 m. Moorings M1_4 and M1_6 are part of a six mooring array deployed in the Laptev Sea continental slope between 2013 and 2015 within the Nansen and Amundsen Basins Observations System II project (NABOS-II). Steric height and bottom pressure equivalent height were calculated from the moorings M1_6 and M1_4 respectively, given that not all measurements were available from a single mooring. M1_4 was composed of one McLane Moored Profiler measuring between 70 m and 760 m, and three CTD sensors at 26 m, 42 m and 53 m. Hereafter, we indicate the combination of data from the two moorings as as M1_4p6. Data are available from the Arctic Data Center, (Polyakov, 2016, 2019; Polyakov and Rembert, 2019).

3.2.2 Velocity

We used measurements of near-surface velocity from two mooring lines to evaluate monthly geostrophic velocity in the Fram Strait and down the continental slope of the Laptev Sea. The Fram Strait array comprises 17 moorings located along a zonal section at 78°50' N, between the longitudes 9° W and 8° E, maintained since 1997 by the AWI (moorings F1–F10 and F15/F16; Beszczynska-Möller et al. (2012)) and the Norwegian Polar Institute (NPI, moorings F11–F14 and F17; de Steur et al. (2009)). Velocity measurements were acquired by Acoustic Doppler Current Profilers (ADCP) and Current Meters (CM). We performed the comparison using the time series recorded by the shallower CM (75 m) and ADCP measurements interpolated to the CM sensor depth. The measurement depth can vary between 75 m and 200 m if the mooring line is slanted by currents. We limited our analysis to the period 2011-2018. Mooring positions and the monthly data availability for the period 2011-2018 are detailed in Table 1. The mooring data are available through PANGAEA (von Appen et al., 2019; von Appen, 2019). For the Laptev

https://doi.org/10.5194/essd-2021-170
Preprint. Discussion started: 25 May 2021

Open Access Earth System Science Data Discussions

Table 1. Names, position and monthly data availability from the moorings along the Fram Strait array. Variable positions indicate the relocation of the moorings in some years. In the third column, values in parenthesis indicate the years of data availability.

Name	Longitude	Latitude	num. months (years)
F1	8°40' E	78°50' N	7 (2015)
F2	8°20' E	78°49'–79°00' N	42 (2011-2012,2015-2018)
F3	8°00' E	78°50'–79°00' N	73 (2011-2018)
F4	7°01' E	78°50'–79°00' N	71 (2011-2018)
F5	5°40'–6°01' E	78°50'–79°00' N	73 (2011-2018)
F6	4°20'–5°00' E	78°50'–79°00' N	34 (2015-2018)
F7	4°00'–4°05' E	78°50' N	38 (2012-2015)
F8	2°45'–2°48' E	78°50' N	25 (2012-2014)
F15	1°35'–1°36' E	78°50' N	42 (2011-2014)
F16	0°00'–0°26' E	78°50' N	70 (2011-2014, 2016-2018)
F9	0°49' W	78°50' N	21 (2011-2012, 2014)
F10	2°03'–1°59' W	78°50' N	68 (2011-2016)
F11	3°04' W	78°48' N	9 (2011-2012)
F12	4°01'–3°59' W	78°48' N	13 (2011-2012)
F13	5°00' W	78°50' N	20 (2011-2012)
F14	6°30' W	78°49' N	12 (2011-2012)
F17	8°7 ' W	78°50' N	13 (2011-2012)

Sea, data were used from four (out of six) moorings deployed in a meridional transect along the 126° E meridian within the context of the NABOS-II project (moorings M1_1 to M1_4). ADCP velocity measurements were averaged in the upper 50 m. These deployments have been carried out twice, in 2013 and 2015. Moorings were respectively recovered in 2015 and 2018, providing a record spanning 5 years (data are available from the Arctic Data Center, Polyakov (2016, 2019); Polyakov and Rembert (2019)). Moorings positions and the monthly data availability are detailed in Table 2.

https://doi.org/10.5194/essd-2021-170
Preprint. Discussion started: 25 May 2021

Open Access Earth System Science Data Discussions

Table 2. Names, position, monthly data availability and depth range over which ADCP data were averaged, for the mooring array along the Laptev Sea continental slope. Variable positions indicate the relocation of the moorings in some years. In the third column, values in parenthesis indicate the years of data availability.

Name	Longitude	Latitude	num. months (years)	Used depth range (m)
M1_1	125°48'–125°50' E	77°04' N	62 (2013-2018)	30-50
M1_2	125°48' E	77°10' N	60 (2013-2018)	10-50
M1_3	125°48' E	77°39' N	61 (2013-2018)	10-50
M1_4	125°54'–125°58' E	78°28' N	61 (2013-2018)	10-50

3.3 Finite Elements Sea ice-Ocean Model (FESOM) output

The decorrelation length scale used for the interpolation of along-track sea surface height was determined based on model data. We used monthly geostrophic velocity derived from sea surface height outputs of the Finite Elements Sea ice-Ocean Model (FESOM) version 1.4. FESOM 1.4 is a coupled sea ice - ocean model, working on a triangular unstructured mesh. The model has a resolution of 4.5 km over the Arctic Ocean and has been described and validated by Wang et al. (2018) and Wang et al. (2019). The run used in this work is the historical run described by Wang et al. (2020), forced by atmospheric reanalysis data of JRA55-do v.1.3 (Tsujino et al., 2018).

4 Methods

In this section we provide a description of the in-situ data processing (Sect 4.1) and of the steps followed to derive altimetry monthly fields from along-track satellite measurements (Sect. 4.2, 4.3 and 4.4). In the last two subsections we provide details on how we performed the comparisons with independent datasets and how we computed the seasonal cycle (Sect. 4.5, 4.6).

4.1 Processing of in situ data

In-situ steric height anomaly (η'_S) and bottom pressure equivalent height anomaly (η'_P) were computed from measurements of water density and ocean bottom pressure. The relation between η' and the time anomaly of *i)* the vertical density profile ($\rho'(z)$) and *ii)* the ocean bottom pressure (P'_b), is derived by integration of the hydrostatic balance from the sea surface down to the bottom depth, D (Eq. 5):

$$P'_b = \rho_0 g \eta' + g \int_{-D}^{0} \rho'(z) dz \tag{5}$$

https://doi.org/10.5194/essd-2021-170
Preprint. Discussion started: 25 May 2021


Open Access Earth System Science Data Discussions

where g is the gravitational acceleration and ρ_0 is a reference ocean water density, set to 1028 kg m^{-3}. Based on this relation, we defined η'_S and η'_P as (Eq. 6):

$$\begin{cases} \eta'_S = -\frac{1}{\rho_0}\int_{-H}^{0}\rho'(z)dz \\ \eta'_P = \frac{P'_b}{\rho_0 g} \end{cases} \quad (6)$$

We computed η'_S and η'_P from measurements of $\rho'(z)$ and P'_b, at the FS_S, AC and M1_4p6 mooring positions. Vertical profiles, $\rho'(z)$, were obtained from temperature and salinity profiles using the UNESCO (1983) formula for density. In turn, temperature and salinity profiles were obtained from moored-sensor data by linear interpolation on a regular pressure grid (2 dbar) between the shallowest sensor (FS_S = 50 m, AC = 50 m, M1_4p6 = 26 m) and the deepest sensor (FS_S = 729 m, AC = 1448 m, M1_4p6 = 700 m). Data was extrapolated from the shallowest sensor to the sea surface assuming constant temperature and salinity, and equal to the uppermost measurement. Below the deepest sensor we assumed the density anomaly to be zero and did not perform extrapolation to the bottom. This conservative approach might have resulted in the underestimation of η'_S. Ocean bottom pressure records P'_b were de-tided using the Matlab function t_tide (Pawlowicz et al., 2002) and instrumental drifts were removed. Unfortunately the time series at FS_S exhibited large pressure anomalies, developing on timescales of several months, whose amplitude was at least one order of magnitude too large to be explained by changes in ocean currents. Therefore, we high-pass filtered this time series with a cutoff frequency of 2 months. All other bottom pressure time series were not affected.

4.2 Along-track sea surface height anomaly

We generated an Arctic-wide dataset of along-track η' by merging the AWI and RADS η' datasets. Inconsistencies between the two datasets were reduced by: i) creating a uniform along-track sampling, ii) reducing biases due to different retracking algorithms, and iii) substituting geophysical corrections where two different corrections were used in the two source products. Here we first give details about these methods and present an estimate of the η' observational uncertainty at the end of the section.

4.2.1 Merging leads and open ocean data

Prior to merging the AWI and RADS datasets we standardized their along-track sampling rates, which originally were respectively 300 m and 7 km. With this aim, the AWI dataset was first smoothed with a moving window of 7 km and then linearly interpolated, following time, onto equally spaced locations (7 km) along the satellite tracks.

A step-like variation in the η' observations at ocean-ice transitions appeared because different models are used to retrack signal returns in ice-covered and ice-free regions (Fig. 2). This is commonly referred to as the "lead-open ocean bias" (Giles et al., 2012). Due to the technical nature of this bias, it is difficult to determine the true bias in this post processing phase. Therefore, we simply removed the offset in η' between leads and open ocean data, estimated directly from the along-track η'. To do so, we identified along-track transitions between the AWI and RADS datasets where the gap was shorter than 200 km. Then we selected observations from the two datasets within an along-track distance of 200 km from the last ice-covered data

https://doi.org/10.5194/essd-2021-170
Preprint. Discussion started: 25 May 2021

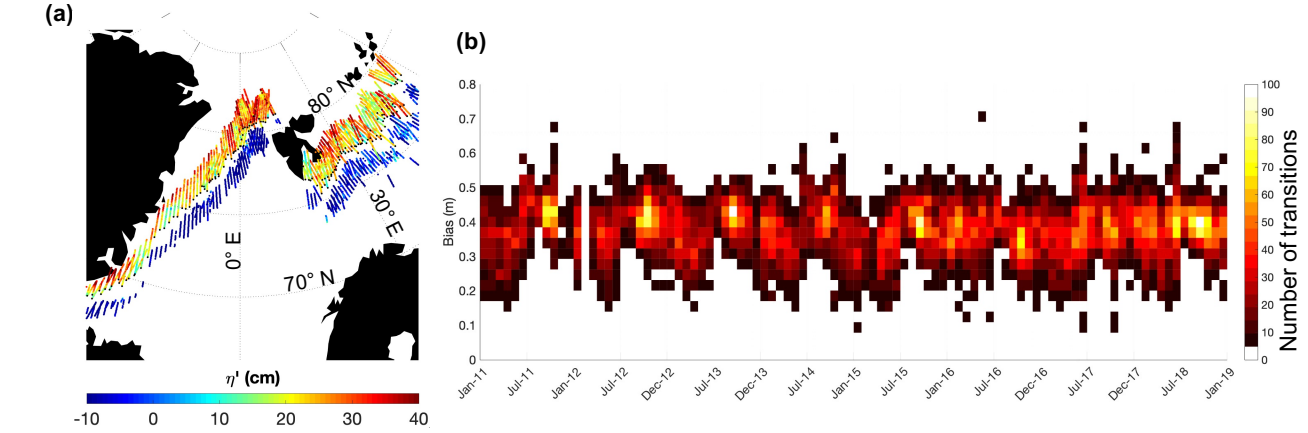

Figure 2. Bias in the η' data in the ice-covered (AWI) relative to the ice-free (RADS) regions. Panel (a) shows data points at the along-track transitions between the AWI and RADS datasets in April 2011 (along-track distance of 200 km on each side) before removing the bias. Black dots indicate the ice edge. Panel (b) shows the temporal evolution of the bias for the period 2011-2018. Note the minimum spread and highest mean of the bias is observed in summer (July to September).

point (Fig. 2a). We calculated the offset at each transition as the difference between the mean values of the selected ice-covered and ice-free η' observations. The offset distribution is different by season (Fig. 2b), but no sensitivity was shown to the ocean-ice transition direction or to the gap between last ocean and first ice data points. Accordingly, we derived monthly offset values as the median of the offsets in that month.

4.2.2 Corrections

As second step, we checked that all corrections applied to the satellite range R (Eq. 1) were consistent between ice-covered and ice-free regions (Table 3 lists the products used here). Standard corrections (European Space Agency, 2016) were applied to both regions to account for i) the reduction in satellite signal speed caused by the presence of the atmosphere (dry gases, water vapour, ions); ii) the difference in reflection properties of wave troughs and crests at the sea surface (sea state bias correction, applied solely in the open ocean); and iii) solid earth tides and ocean tides.

A further correction removes the high frequency ocean response to atmospheric pressure and wind forcing. For ice-covered regions ESA suggests using an Inverted Barometer (IB) formula. Here instead, we applied the Dynamic Atmosphere Correction (DAC, Carrère and Lyard (2003); Carrère et al. (2016)) to both, ice-covered and ice-free regions. DAC is conventionally used in the global ocean because it better suppresses high frequency variability, avoiding aliasing of sub-monthly temporal changes into spatial variability (Carrère and Lyard, 2003; Quinn and Ponte, 2012; Carrère et al., 2016).

No study to date shows which of the DAC and IB corrections performs better in ice-covered regions. However, gaining insight into this issue was relevant to us because residual sub-monthly variability emerges in the monthly η' fields as meridionally elongated patterns (meridional "trackiness", Stammer et al. (2000)). Therefore, to support our choice of using DAC over IB,

https://doi.org/10.5194/essd-2021-170
Preprint. Discussion started: 25 May 2021

Open Access Earth System Science Data Discussions

Table 3. Altimetry corrections applied in this study. Acronyms: ECMWF (European Centre for Medium-range Weather Forecast); CNES (Centre National d'Etudes Spatiales); MOG2D (Modèle d'ondes de gravité 2D); FES2004 (Finite Element Solution 2004); GDR-E (Geophysical Data Record, version E).

Correction	Source	References
Dry troposphere	derived from mean surface pressure, based on the ECMWF model	European Space Agency (2016)
Wet troposphere	derived from mean surface pressure, based on the ECMWF model	European Space Agency (2016)
Ionosphere	Global Ionospheric Map, provided by CNES	Komjathy and Born (1999)
Dynamic Atmosphere	Inverted Barometer + MOG2D barotropic model	Carrère et al. (2016)
Sea State Bias (only open ocean)	Hybrid (mix between parametric and non-parametric techniques)	Scharroo and Lillibridge (2005)
Ocean Tide	FES2004	Lyard et al. (2006)
Solid Earth Tide	Cartwright model	Cartwright and Edden (1973)
Geocentric Polar Tide	Instantaneous Polar Location files (sourced from CNES)	Wahr (1985)
Orbit	GDR-E	European Space Agency (2016)

we looked at which of them reduced the η' standard deviation the most with respect to the uncorrected η' (see Appendix A). Results showed that DAC outperforms the IB in shallow shelf regions (particularly the East Siberian Sea and the Chukchi Sea) and that they perform equally well over the deep basins (Fig. A1). For instance, in the East Siberian Sea the DAC reduced the uncorrected η' standard deviation by 50% at periods shorter than 20 days, in contrast to no reduction when applying a simple IB (see Table A1). The improvement of DAC with respect to IB over the shelves appears also in the η' monthly grids, where meridionally oriented patterns of η' are evidently reduced (two examples are given for the months of November 2014 and November 2017 in Fig. A2).

4.2.3 Final along-track dataset and uncertainty estimate

Following the steps above we generated a final merged along-track dataset, composed of two sub-datasets; one for the ice-covered region and one for the ice-free region. The consistency of these two sub-datasets is indicated by their comparable Arctic-wide standard deviation over the period 2011-2018 (10.4 cm and 10.5 cm, respectively). An example is illustrated for the month of July 2015 in Fig. 3, which shows a smooth transition between the two sub-datasets. We note though, there is some residual sub-monthly variability. For instance, Fig. 3a shows a decrease of η' of $\sim$20 cm north of Greenland between the first and the fourth week of July 2015. The residual sub-monthly variability is one of the two main contributions to the error on

https://doi.org/10.5194/essd-2021-170
Preprint. Discussion started: 25 May 2021

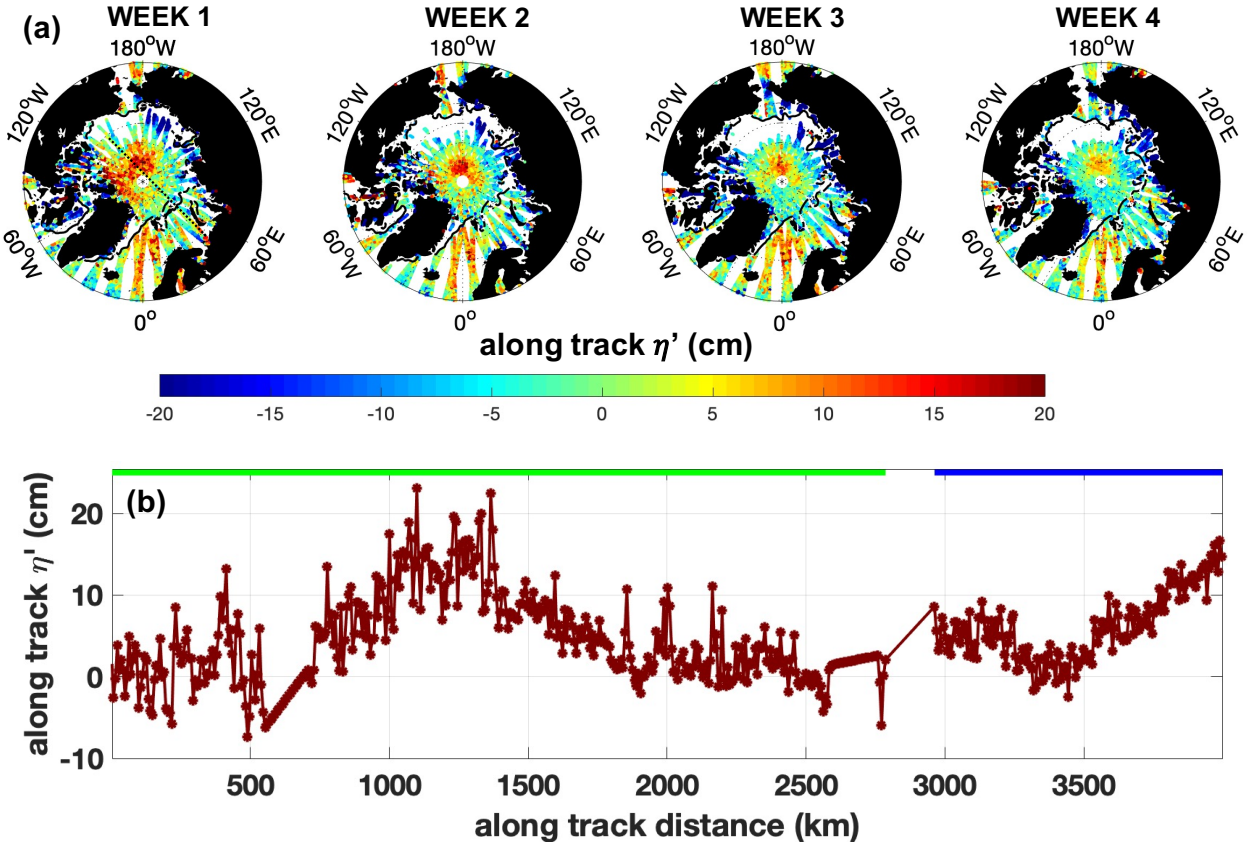

Figure 3. Example of the along-track η' dataset covering the ice-covered and ice-free Arctic Ocean. (a) The weekly availability of along-track data in the month of July 2015 (weeks defined as days 1-8, 9-15,16-23,24-31). The black solid line indicates the 15% sea ice concentration as derived from the OSI SAF ice concentration products (archive OSI-401-b, available at ftp://osisaf.met.no/archive/ice/conc/). (b) η' along the satellite track indicated with a dashed black line in panel (a) (track passing over the Arctic Ocean on the 1st of July 2015, between 16:00 and 17:00 UTC). The distance along the track goas from the Canada Basin towards the coasts of Russia. Data in ice-covered areas are marked by a green line and data from the ice-free areas by a blue line.

the monthly η' fields. This contribution is estimated as part of the processing algorithm during the interpolation phase (Sect. 4.3.3). The second contributor to the error is the observational uncertainty.

The observational uncertainty associated to the along-track η' stems from several sources, namely the altimeter measurement uncertainty, the waveform retracking method, the corrections and orbit uncertainty. Given the difficulty of assessing the
240 contribution of each of these sources, we provide here a comprehensive estimate of the observational uncertainty based on the differences of the along-track η' at satellite tracks crossovers (Fig. 4). We first defined crossovers as those pairs of η' observations within a distance of 7 km. We excluded pairs belonging to the same satellite pass by verifying that they are separated by more than one hour. Considering the large number of data, we organised observations in an equal area grid of about 100 km

https://doi.org/10.5194/essd-2021-170
Preprint. Discussion started: 25 May 2021

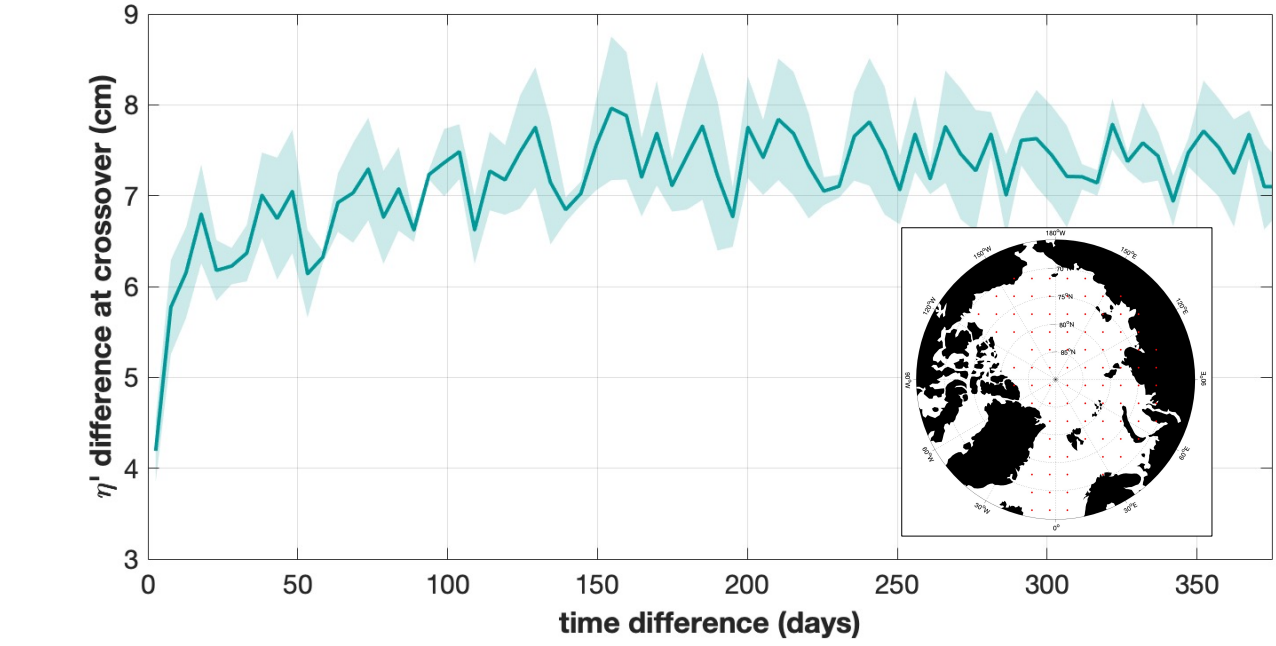

Figure 4. η' difference at crossovers for satellite tracks crossing in a period of time up to 1 year. The solid line in the main panel is the crossover difference averaged every 5 days; the shaded area shows the standard deviation of crossover differences averaged every 1 day. Crossovers differences have been computed within 100 km around the locations indicated in the inset panel.

and computed the η' differences at crossovers only within selected cells (red dots in the inset of Fig. 4). We expect that the η' differences tend to the observational uncertainty as the crossovers get closer in time. Thus our uncertainty estimate was given by the average η' difference at crossovers separated by no more than 5 days, which is 4.2 cm.

This analysis provides additional information about the η' de-correlation time scale. The η' crossover difference increases with time above the uncertainty due to local variability. Fig. 4 shows that variability increases by $\sim$2 cm in the first 20 days, then by a further $\sim$1 cm after 6 months, until it finally reaches a plateau. This indicates that, at time scales shorter than one year, η' has a short de-correlation time scale of 20 days and a long de-correlation time scale of 6 months.

4.3 Gridded sea surface height anomaly

We produced monthly η' fields over the period 2011-2018, by interpolation of the along-track data onto a longitude-latitude grid of resolution 0.75°×0.25°, from 60° N to 88° N. Gridding creates regular fields from irregularly distributed data points. Below we first describe the technique used to reduce residual sub-monthly variability in the along-track η' (Sect. 4.3.1). Then give details about the interpolation method used, including the selection of the length scale and signal to noise ratio (Sect. 4.3.2). Finally we provide an estimate of the standard error of the monthly η' fields (Sect. 4.3.3).

https://doi.org/10.5194/essd-2021-170
Preprint. Discussion started: 25 May 2021

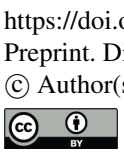

Open Access Earth System Science Data Discussions

4.3.1 Minimisation of sub-monthly variability

The residual sub-monthly variability (described in Sec. 4.2.3) produces marked meridional trackiness if the interpolation is performed on a monthly set of η' observations (see Fig. 5a, July 2015). To reduce this variability we performed the interpolation on weekly data subsets instead. The monthly maps were then obtained as the average of four weekly maps, with the associated error given by the quadratic sum of the weekly error maps (shown below in Fig. 6). Fig. 5b shows data along a latitude circle as an example of the trackiness reduction obtained thanks to this approach. Fig. 5c shows the contribution of the sub-monthly variability to the error on the monthly η' fields and it is explained below in Sect. 4.3.3.

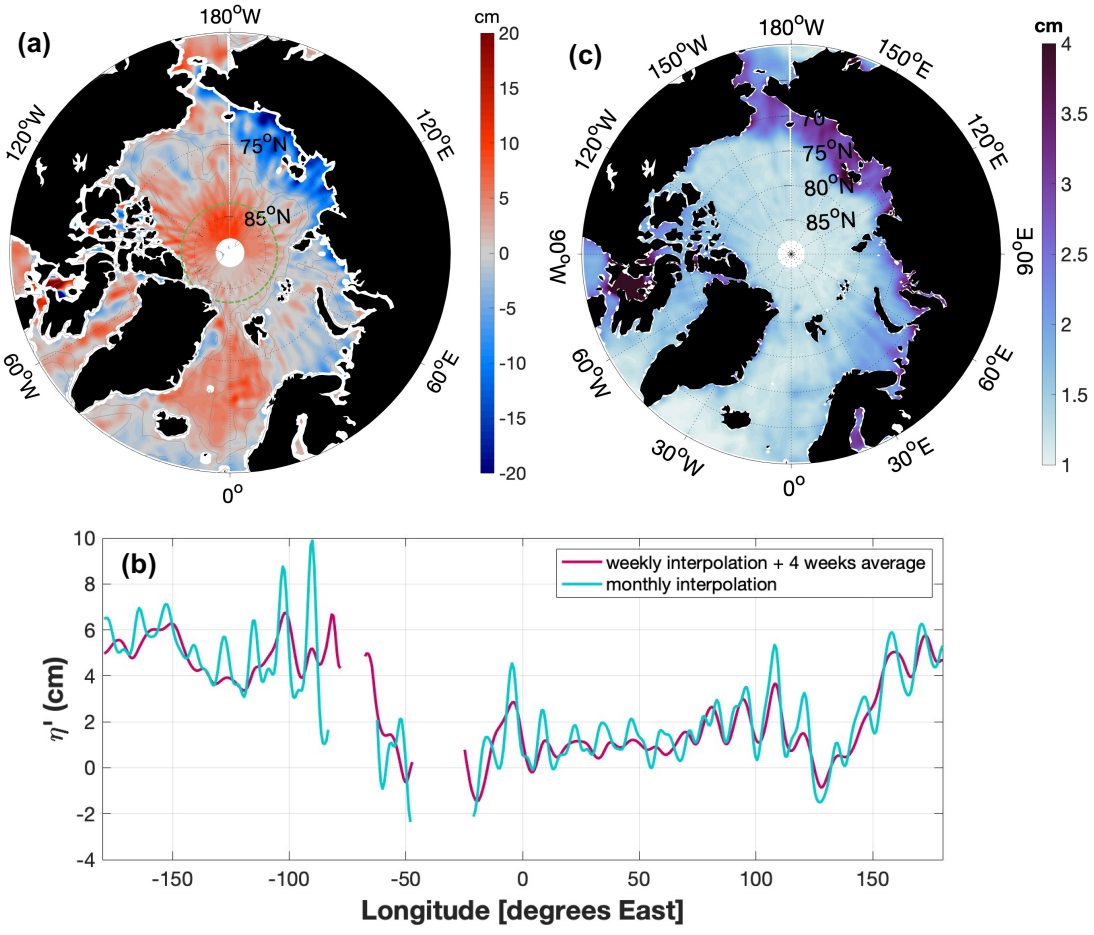

Figure 5. Residual sub-monthly variability in the η' observations and gridded field. (a) The July 2015 monthly gridded η' field obtained by interpolation performed on monthly data input. (b) η' along a latitude (83° N) circle; η' obtained from weekly and monthly interpolations are shown with magenta and cyan lines, respectively. (c) The sub-monthly contribution to the standard error on monthly η' maps, averaged over the period 2011-2018. In panel (a) bathymetry contours are drawn at 100 m, 1000 m and 2500 m depth.

https://doi.org/10.5194/essd-2021-170
Preprint. Discussion started: 25 May 2021

Open Access Earth System Science Data Discussions

4.3.2 Interpolation via DIVA

In oceanography, regular fields are commonly created via a technique called optimal interpolation (Bretherton et al., 1976). This approach though, has the disadvantage of generating the interpolated field based on an a priori functional form of the covariance between data points. The variational inverse method that we use here is an alternative which does not assume an a priori behaviour of the analysed field. Instead, it improves the quality of the interpolated field (e.g., closeness to data, smoothness), by minimizing a cost function dependent on the data and few input parameters (Troupin et al., 2012). An additional advantage of this method is that it decouples ocean basins separated by land by minimizing the cost function on a finite elements mesh, whose nodes are not connected across land.

We used a specific realization of the variational inverse method, namely the Data-Interpolating Variational Analysis (DIVA, Troupin et al. (2012)). Further information is provided in Appendix B. As input to DIVA, the along-track η' data and two parameters, the length scale L and the data signal to noise ratio λ are provided. DIVA gives the possibility to introduce an anisotropic weighting of the data points, which we tested via an input vector field.

The selection of values for λ and L was done as follows. First we carried out twenty interpolation runs with λ =0.1, 0.3, 1, 10 and L =20 km, 50 km, 100 km, 300 km, 600 km. These values of λ cover the cases when $a)$ data contain little information with respect to the noise level or the data are not representative of the monthly mean (λ =0.1), and $b)$ when the noise level is only 10% of a real signal (λ =10). The range of length scales L covers Arctic Ocean circulation scales, from mesoscale dynamics to basin wide flow (e.g., Nurser and Bacon, 2014; Armitage et al., 2016). Since λ and L are the main input parameters for the interpolation, we did not include the anisotropic weighting initially, but its effect was tested separately at a later stage (described below).

Next, we compared the results of each interpolation run with two independent datasets:

- $\eta'_P + \eta'_S$ time series at the FS_S, AC and M1_4p6 moorings (Sect. 3.2.1);
- average geostrophic transport from the FESOM model outputs (Sect. 3.3), normal to two transects; one crossing the opening of the Laptev Sea into the Eurasian Basin and another across the north-western Fram Strait (both transects are indicated in Fig. 1).

The aim of these comparisons was to select the λ and L values whose interpolated field best captured $i)$ the high temporal resolution patterns exhibited by the in-situ data and $ii)$ the large scale features simulated by the model.

The comparisons were assessed by defining a score $S(\lambda, L)$, such that (Eq. 7):

$$S(\lambda, L) = \frac{1}{5} \sum_i \left[(1 - C_i(\lambda, L)) + \frac{\mathrm{RMSD}_i(\lambda, L)}{X_{i,max} - X_{i,min}} \right] \tag{7}$$

where $C_i(\lambda, L)$ represents the correlation of a given run (with parameters λ and L) with the in-situ or model time series i; $\mathrm{RMSD}_i(\lambda, L)$ is the root mean square difference between each run and the time series i; and $X_{i,max}$ and $X_{i,min}$ are the maximum and minimum values of the interpolation (either η' or (u_g, v_g)) in each comparison. This score is designed to be

https://doi.org/10.5194/essd-2021-170
Preprint. Discussion started: 25 May 2021

Open Access Earth System Science Data Discussions

Table 4. Scores of interpolation runs (as expressed in Eq. 7) using different length scale L and signal-to-noise ration λ.

	L = 20 km	L = 50 km	L = 100 km	L = 300 km	L = 600 km
$\lambda = 0.1$	0.822	0.756	0.766	0.803	0.839
$\lambda = 0.3$	0.788	0.752	0.764	0.797	0.820
$\lambda = 1$	0.779	0.749	0.752	0.776	0.813
$\lambda = 10$	0.787	0.772	0.762	0.773	0.805

minimum for the best agreement with the independent datasets. Each term in S is normalised so that it has a similar relative weight.

The scores (S) are presented in Table 4. They vary only by a small fraction, indicating that the patterns in the altimeter fields are insensitive to the choice of parameter values. There is though, a minimum score for $\lambda = 1$ and $L = 50$ km, which were thus selected as a suitable set of parameter values.

Finally, we tested the anisotropic weighting (Eq. B3) by including it in interpolation runs with the selected λ and L. As vector field we used the long-term mean (1992-2012) geostrophic velocity field from the FESOM model. We used two amplification factors a ($a = 100$, $a = 10^6$) to represent the effect of weak or strong advection. Results showed the effect of advection of η' by the mean flow to be negligible, even with high a. Therefore, we did not apply this constraint to compute the final η' gridded fields.

The error maps associated with the interpolation were provided by DIVA through the poorman's estimate method (Troupin et al., 2012). This method circumvents the high computational cost of calculating the real covariance in DIVA by assuming a constant covariance between data points. The poorman's estimate method generates maps of relative error, given as fraction of the variance of the background field (Troupin et al., 2012). These maps allow to assess the data coverage given by the distribution of the data in space scaled by the decorrelation scale L. An approximate way to scale the relative error to observational units is by multiplication with the standard deviation of the input data. For the final product we provide the relative error maps.

4.3.3 Error on monthly fields

The error in the monthly η' fields comprises a component arising from the observational uncertainty and another arising from the sub-monthly variability. The error arising from the observational uncertainty varies spatially depending on the data distribution and the interpolation method. However, given that the poorman's estimate method does not provide an estimate of the absolute error, we used an alternative procedure to yield an average estimate of the standard error components over the entire Arctic Ocean. The components of the domain-averaged standard error were computed for each month as follows. The component deriving from the observational uncertainty was obtained by dividing the uncertainty estimate of an individual measurement (i.e. 4.2 cm, Sect. 4.2.3) by the square root of the average number of data points per cell. The component

https://doi.org/10.5194/essd-2021-170
Preprint. Discussion started: 25 May 2021

stemming from the sub-monthly variability was calculated at each grid point as the standard deviation of the four weekly η' maps divided by the square root of four, and then averaged across the Arctic. The monthly standard error contributions arising from the observational uncertainty and the sub-monthly variability, averaged over the period 2011-2018, amount respectively to 1.7 cm and 1.8 cm. The two components contribute equally to the total monthly standard error over the period 2011-2018, which is 3.5 cm. The spatial distribution of the time-averaged sub-monthly contribution is shown in Fig 5c. This varies between 1 and 4 cm. Values between 1 and 2 cm are found in areas deeper than 100 m and values above 3 cm are found along the coasts of the Barents, Kara and Laptev Seas, in the East Siberian and Chukchi Seas, and in the southern Canadian Arctic Archipelago.

4.4 Gridded geostrophic velocity

The geostrophic velocity was computed on the output grid following Eq. 4, with partial derivatives approximated by finite differences. The components of velocity on the longitude-latitude grid at indices i, j are given by (Eq. 8):

$$\begin{cases} u_{g,ij} = -\frac{g}{f_0 R_e} \cdot \frac{\eta_{i+1,j} - \eta_{i-1,j}}{\theta_{i+1,j} - \theta_{i-1,j}} \\ v_{g,ij} = \frac{g}{f_0 R_e} \cdot \frac{1}{cos(\theta_{ij})} \cdot \frac{\eta_{i+1,j} - \eta_{i-1,j}}{\Phi_{i+1,j} - \Phi_{i-1,j}} \end{cases} \tag{8}$$

where θ and Φ are latitude and longitude converted to radian angles, $f = 2\Omega sin(\theta)$ is the Coriolis parameter (with $\Omega = 7.29 \cdot 10^{-5}$ s^{-1}) and R_e is the Earth radius. In the equation above, $\eta_{i,j}$ is the η field at indices i, j obtained by adding the gridded η' to the DTU17MDT linearly interpolated to the grid.

4.5 Comparison to independent datasets

The monthly η' maps were first evaluated over the whole Arctic Ocean by comparison to the CPOM DOT product. The comparison was done at grid points south of 82º N (the northernmost latitude covered by the CPOM DOT), for the period January 2011 to December 2014. Both datasets were referred to their own temporal average over this period.

In the next step we evaluated our η' fields locally via comparison with time series of in-situ sea surface height $\eta'_i = \eta'_P + \eta'_S$ (Eq. 5 and 6) from moorings FS_S, AC and M1_4p6. The altimetry η' was linearly interpolated to the in-situ locations, and the time average over the period of mooring deployments were removed from in-situ and altimetry observations.

Lastly, we assessed geostrophic current fields (u_g, v_g) by comparison to in-situ measured currents from the two mooring lines crossing the Fram Strait and the Laptev Sea continental slope. We compared the (u_g, v_g) component normal to the transects, linearly interpolated to the moorings positions, to monthly averages of the in-situ measured velocities normal to the transects. These are hereafter referred to as v_n and v_{ni} respectively, positive northward in the Fram Strait and eastward in the Laptev Sea. The comparison was limited to those mooring locations where more than 24 months of in-situ data were available at the time of manuscript preparation.

To establish spatial scales over which altimetry-derived currents approximate best the in-situ measured currents, we compared v_n and v_{ni} spatially averaged over different sets of neighbouring moorings. The averaging was performed by assigning to each mooring a weight proportional to its distance to the two neighbouring moorings (e.g., for mooring j: $w_j = \frac{d_{j-1,j} + d_{j,j+1}}{2}$, where d is the distance). We performed three tests in the Fram Strait and two at the Laptev Sea continental slope, using moor-

https://doi.org/10.5194/essd-2021-170
Preprint. Discussion started: 25 May 2021

350 ings closest to the shelf break (tests 1 to 5). We evaluated the improvement of each test based on the results at those moorings where the pointwise correlation was highest. Finally, we looked at which time scales are dominant in each dataset. To do so, we evaluated the percentage of variance explained by the seasonal to interannual frequency band (lower than 4 months) and by the intra-annual frequency band (higher than 4 months) as (Eq. 9):

$$E = 100 \cdot (1 - \frac{var(x - x_F)}{var(x)}) \tag{9}$$

355 where x is the horizontally averaged velocity time series (tests 1 to 5), and x_F is the correspondent filtered time series.

4.6 Seasonal cycle

The seasonality of the Arctic sea level and surface currents has been studied in several previous works (e.g., Volkov et al., 2013; Armitage et al., 2016; Beszczynska-Möller et al., 2012; Baumann et al., 2018), giving us the opportunity to assess our dataset based on this literature. We defined the seasonal cycle of η', following Volkov et al. (2013), as the harmonic least-square fit to
360 η' with period of one year (Eq. 10):

$$\eta'_{seas} = A \cdot cos\left[2\pi\left(\frac{t-\alpha}{P}\right)\right] \tag{10}$$

where t is the number of the month in the time series ($t = 1$ correspond to January 2011) and $P = 12$ is the oscillation period. We evaluated the fraction of variance explained by η'_{seas} at each grid point following Eq. 9, with η' as x and η'_{seas} as x_F.

5 Results

365 Here we first describe the characteristics of the η' and geostrophic velocity (u_g, v_g) monthly maps, then show the results of their comparison against independent datasets, and lastly present the η' and (u_g, v_g) seasonal cycle.

5.1 Monthly fields of sea surface height anomaly and geostrophic velocity

Given our data set spans 96 months within the 2011-2018 period, here we present results from the month of July 2015 as an example to describe general characteristics of a given map. Fig. 6 shows fields of η', relative error (associated with the
370 interpolation) and (u_g, v_g) for July 2015. The description below makes reference to the Arctic Ocean sub-regions and long term mean surface circulation pathways presented in Fig. 1.

In the η' monthly fields we find that there are extended regions of either positive or negative values. From Fig. 6a for instance, it can be appreciated that η' is positive in the Nordic Seas and across the Arctic Deep Basins, but negative over the Eurasian Shelves. η' also varies within these regions, being maximum ($\sim$10 cm) north of 85° N, and minimum in the Laptev
375 Sea. Superimposed on these large scale patterns, residual meridional trackiness appears south of 80° N, especially in shallow areas, where the error related to sub-monthly variability is relatively high (Fig. 5c). For example, enhanced trackiness is visible in the Barents Sea, where previous work has shown that intra-seasonal sea surface height variability explains between 50% and 80% of the total variability (Volkov et al., 2013).

https://doi.org/10.5194/essd-2021-170
Preprint. Discussion started: 25 May 2021

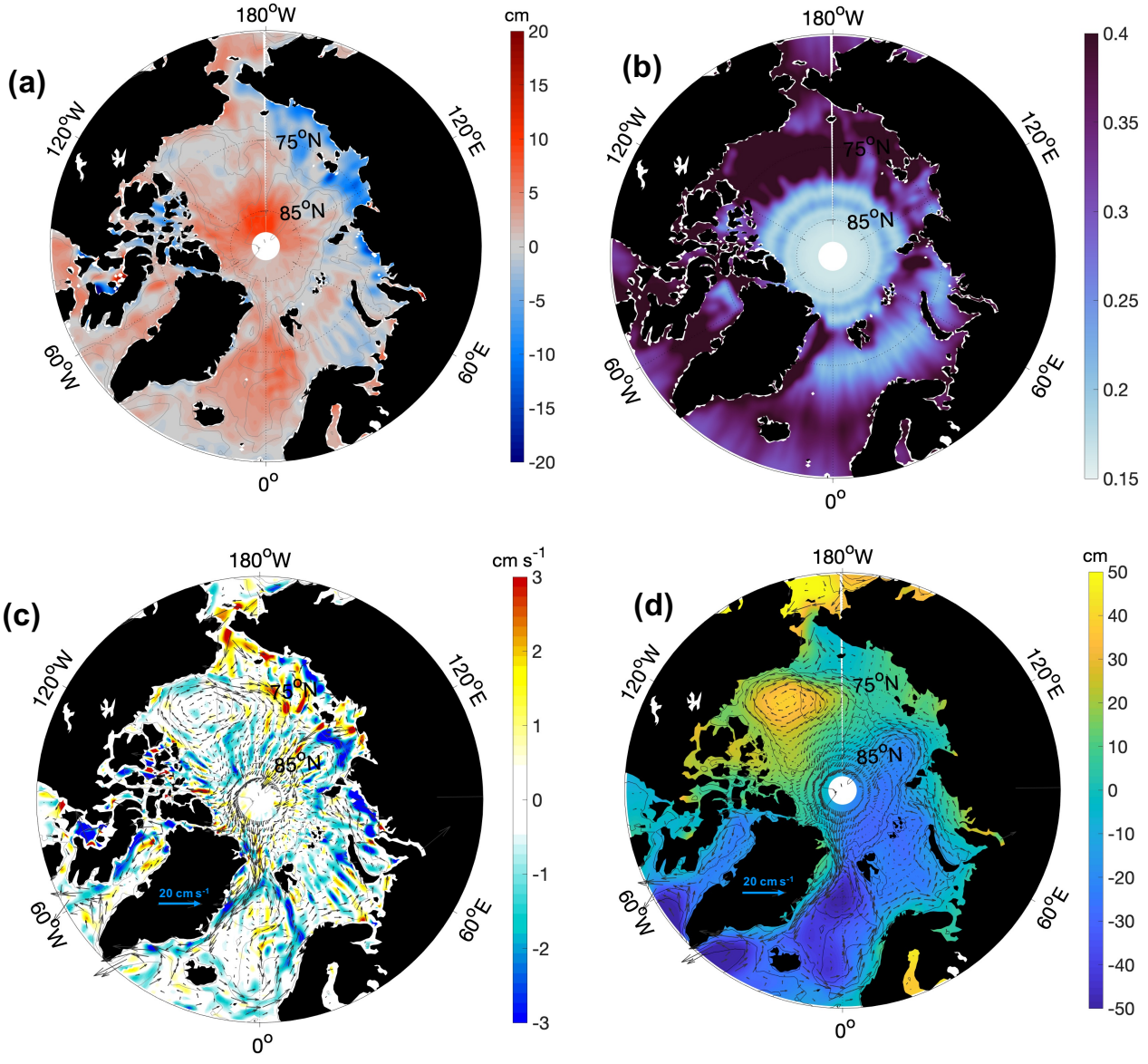

Figure 6. Example of monthly gridded fields provided in the final data product (July 2015). (a) The η' field. (b) Relative error field on the interpolated η'. (c) The (u_g, v_g) field; arrows in (c) represent the absolute (u_g, v_g) field, whereas colour highlights the anomaly of the monthly geostrophic speed ($V_g = \sqrt{u_g^2 + v_g^2}$) with respect to the long term mean geostrophic speed. (d) Mean dynamic topography DTU17MDT (background color) and the DTU17MDT-derived mean geostrophic velocity. In panels (a) and (c), bathymetry contours are drawn at 100 m, 1000 m and 2500 m depth.

https://doi.org/10.5194/essd-2021-170
Preprint. Discussion started: 25 May 2021


Open Access Earth System Science Data Discussions

The relative error for the month of July 2015 is on average 0.27, with a minimum of 0.16 around the North Pole and a maximum of 0.50 in the Southern Canada Basin (Fig. 6b). Largest relative errors are found in regions with data gaps (see data distribution in Fig. 3a): $i)$ south of 75° N, where the distance between the satellite tracks increases considerably; $ii)$ in a zonal band around 80° N, where the weekly data distribution is not uniform due to the satellite orbit geometry; and $iii)$ in the Canada Basin, where there is a large and persistent marginal ice zone. Neither the AWI nor by the RADS processing provide data over marginal ice zones.

In Fig. 6c we present the geostrophic vector field $(u_g, v_{,g})$, with background colors highlighting monthly speed anomalies relative to the DTU17MDT-derived mean velocity. The distribution of anomalies aligns well with known circulation pathways, such as those found along steep bottom topography gradients or large scale current patterns like the Beaufort Gyre and the Transpolar Drift. The map shows that currents around the Nordic Seas (East Greenland Current, West Spitsbergen Current and the Norwegian Atlantic Current) and at the Laptev Sea continental slope (Arctic Circumpolar Boundary Current) are weak, while they are intensified in the westernmost branch of the Beaufort Gyre and in the Pacific Water inflow across the Bering Strait currents. This indicates our data set yields realistic variability over a large span of the Arctic Ocean. Still, there are small areas where speed anomalies appear along meridionally elongated stripes, i.e., not following bottom topography contours. These patterns result from gradients between residual η' sub-monthly variability and do not correspond to real monthly velocity anomaly.

5.2 Comparison to independent datasets

5.2.1 Sea surface height anomaly

Results of the comparison with the CPOM DOT show good agreement over most of the domain, with a correlation between datasets above 0.7 for 62% of the grid points (Fig. 7a). The comparison yields intermediate correlation values (0.3 to 0.7) south of 65ºN, in some areas around the central Arctic, and along the Canadian and Greenland coasts (where the multi year ice persists for most of the year). Only in 2% of the domain the correlation is below 0.3 (central Baffin Bay and northeast Greenland Shelf). The root-mean-square deviation (RMSD) is presented in Fig. 7b, showing low values (2 cm to 4 cm) over 75% of the domain, including most of the regions with water depth greater than 100 m. The RMSD is high (7-8 cm) over the East Siberian Sea and Chukchi Sea, where the sub-monthly variability is most enhanced.

Time series of the comparison of η' with in-situ data are shown in Fig. 8, and the associated RMSD and correlation coefficients are presented in Table 5. The correlation between the η' and η'_i time series is relatively low (0.3 to 0.5), but significant (p-value < 0.05). η' and η'_i follow roughly a similar pattern, varying within a range of $\pm$10 cm over the comparison period at all three sites. At the FS_S mooring there are hints of a seasonal oscillation, with the signal decreasing from October 2016 to March-April 2017 and then increasing towards October 2017 (Fig. 8). At the AC and M1_4p6 moorings short term variability appears in phase at times, for instance between December 2016 and May 2017 in the former, and between September 2014 and February 2015 in the latter (Fig. 8). There are however, differences as large as the altimetry variability in some months, which is reflected in the RMSD and the η' standard deviation (Table 5).

https://doi.org/10.5194/essd-2021-170
Preprint. Discussion started: 25 May 2021

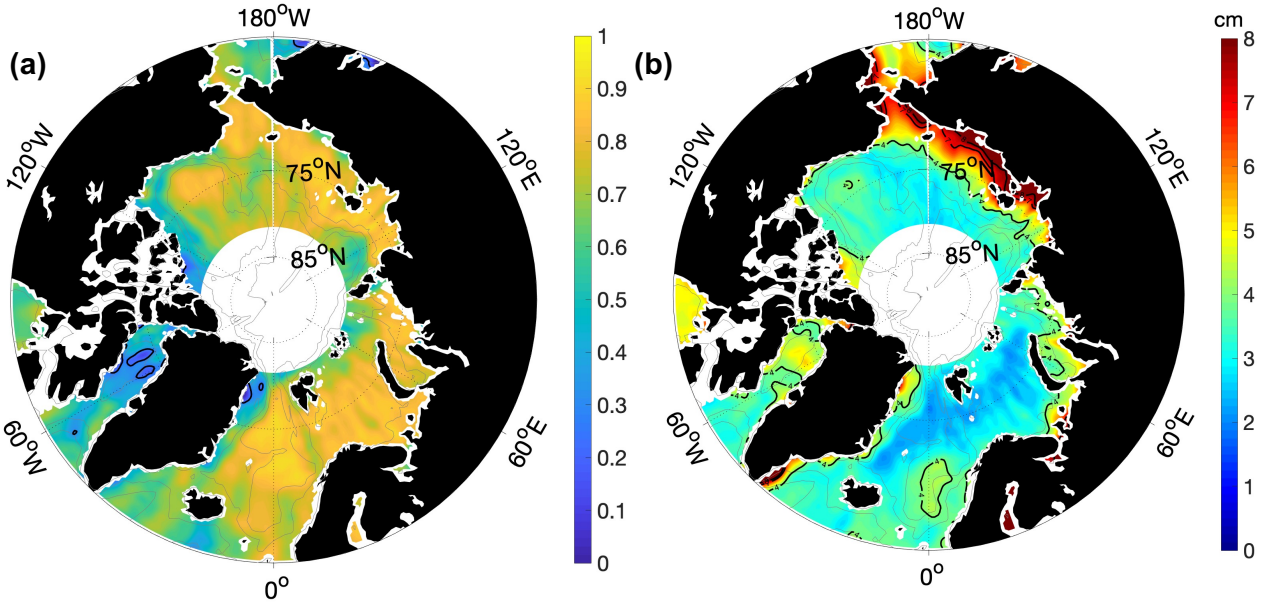

Figure 7. (a) Correlation (Pearson's correlation coefficient) and (b) RMSD between the gridded η' fields as derived in this work and the CPOM DOT published by Armitage et al. (2016). Areas north of 82° N are not covered by the CPOM DOT. In panel (a), areas within the thick black lines show correlations <0.3 and p-values >0.05. In panel (b), thick black lines are contours of 4 cm, 7 cm and 8 cm. Bathymetry contours (dotted lines) are drawn at 100 m, 1000 m and 2500 m depth.

Table 5. Comparison between altimetry and in-situ sea surface height anomaly. The first row show the correlation (Pearson's correlation coefficient, p-values were computed using the effective number of degrees of freedom (Emery and Thomson, 2001)). The second row shows the RMSD between altimetry η' and in-situ η'_i at moorings FS_S, AC and M1_4p6.

	Fram Strait	**Arctic Cape**	**Laptev Sea**
Correlation η'_i (p-value)	0.30 (0.05)	0.42 (<0.01)	0.50 (0.01)
RMSD η'_i [cm]	3.3	3.5	5.4

https://doi.org/10.5194/essd-2021-170
Preprint. Discussion started: 25 May 2021

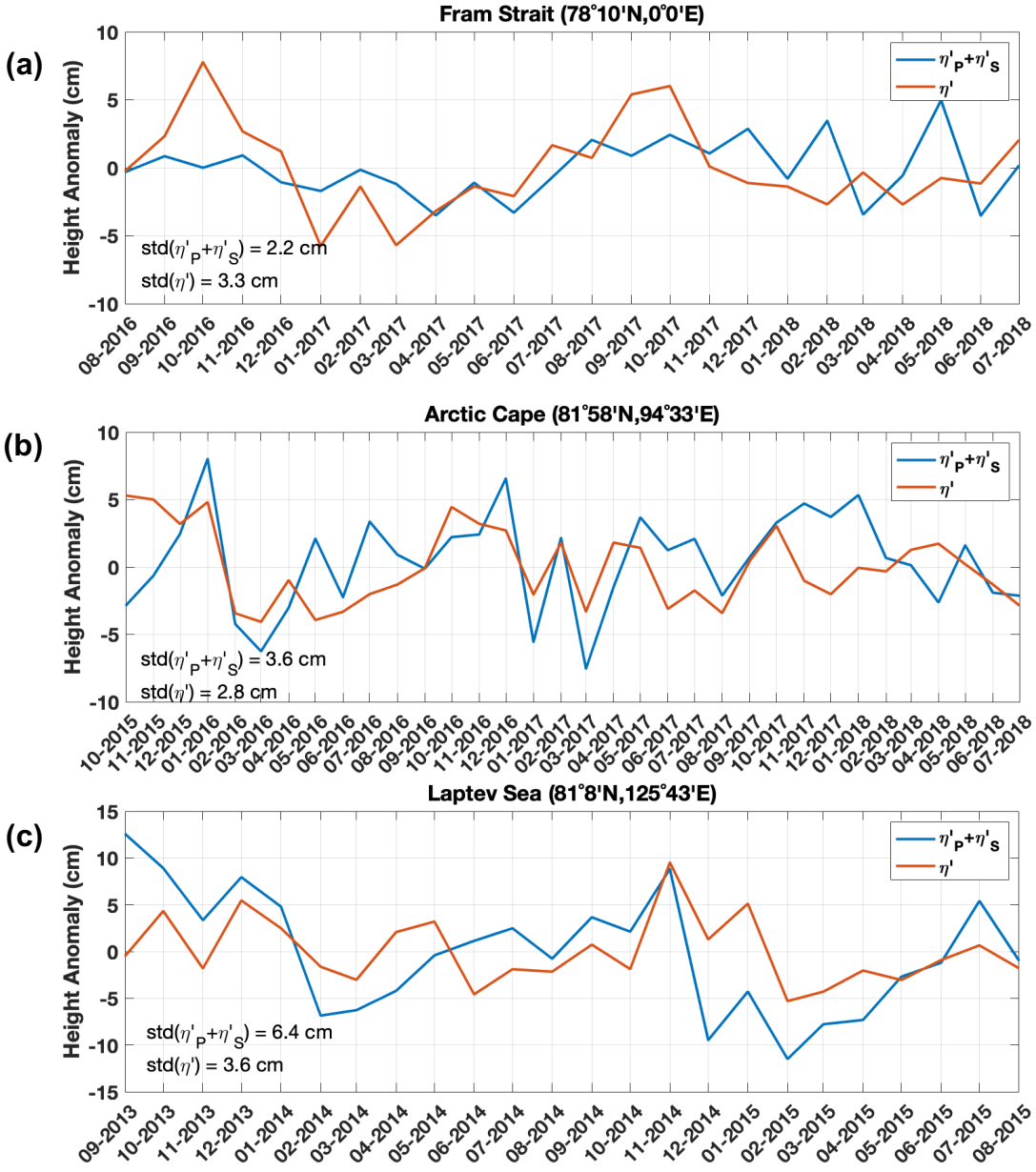

Figure 8. The $\eta_i' = \eta_P' + \eta_S'$ (blue line) derived from in-situ observations at the three moorings (a) FS_S, (b) AC, (c) M1_4p6 is displayed against the η' interpolated at the mooring location (red line). Standard deviations of η' and η_i' are displayed in the bottom left corners.

https://doi.org/10.5194/essd-2021-170
Preprint. Discussion started: 25 May 2021

Open Access Earth System Science Data Discussions

Table 6. Comparison of altimetry and in-situ velocities. The first four rows show the mean and standard deviation of the altimetry-derived v_n and mooring v_{ni} velocities normal to the transects. The next two rows show RMSD and correlation (Pearson's correlation coefficient) between v_n and v_{ni}; correlations with p-value<0.05 are highlighted in bold. P-values were computed using the effective number of degrees of freedom (Emery and Thomson, 2001).

	Fram Strait										**Laptev Sea**			
	F10	F16	F15	F8	F7	F6	F5	F4	F3	F2	M1_1	M1_2	M1_3	M1_4
mean v_n (cm s^{-1})	-9.4	-5.6	-3.5	-1.8	-0.1	0.9	2.3	3.1	3.5	3.5	4.5	4.4	3.9	2.6
mean v_{ni} (cm s^{-1})	-7.9	1.1	-0.8	6.1	-2.5	-2.6	5.3	6.0	17.0	18.1	12.1	3.5	3.4	1.6
std v_n (cm s^{-1})	1.5	1.2	0.9	0.9	0.9	1.0	1.3	1.5	1.5	1.7	2.1	2.0	1.2	0.8
std v_{ni} (cm s^{-1})	5.0	7.1	6.9	5.5	6.9	7.0	6.7	7.2	7.6	7.6	7.4	4.2	1.8	1.2
RMSD (cm s^{-1})	5.0	7.0	6.9	5.6	6.6	6.9	6.3	6.8	6.8	7.0	5.9	4.5	1.9	1.3
Correlation	0.11	0.06	-0.04	-0.14	**0.34**	0.06	**0.34**	**0.32**	**0.53**	**0.38**	**0.77**	0.04	**0.29**	0.24

5.2.2 Velocity

The agreement of in-situ and altimetry-derived velocities is summarized in Table 6, which presents their correlation and RMSD, together with the mean velocities and standard deviation at each mooring (computed over the months when in-situ data were available). Time series across the Fram Strait and Laptev Sea mooring lines are displayed in Fig. 9 and 10. In the Fram Strait, the correlation is significant (p-value < 0.05) and higher than 0.3 at moorings F2 to F5. At these 4 moorings, both the mean v_n and v_{ni} are consistently positive and comparable or higher than the corresponding standard deviation. The correlation was highest at mooring F3; the mooring with the longest continuous time series. In the Laptev Sea continental slope the correlation is highest at the M1_1 mooring. Further down the slope the correlation is lower, being still significant at mooring M1_3, but non-significant at moorings M1_2 and M1_4.

There are differences between altimetry and in-situ data in terms of spatial and temporal resolution. The mean v_n shows low spatial variability and smooth transitions between nearby sites (Table 6). Note that this variability is governed by the averaging scales underlying the DTU17MDT product. The scales captured by the DTU17MDT are defined by the resolution of the geoid model used to compute it. Previous studies indicate that these scales are not smaller than 100-150 km (Gruber and Willberg, 2019; Bruinsma et al., 2014; Farrell et al., 2012). These large scales contrast with the high spatial variability of the v_{ni} mean flow, which is derived by pointwise measurements. This is shown for instance by abrupt changes between moorings F15 and F7 (50 km apart) or between M1_1 and M1_2 (11 km apart). High spatial variability observed by the mooring data is ascribable to the small Arctic first baroclinic Rossby radius, which is below 10 km in the two study regions (Nurser and Bacon, 2014; von

https://doi.org/10.5194/essd-2021-170
Preprint. Discussion started: 25 May 2021

Table 7. Comparison of spatially averaged altimetry and in-situ velocities. The first two rows show the correlation (Pearson's correlation coefficient) and RMSD between horizontally averaged v_n and v_{ni}. Each test corresponds to the averaging of two or more moorings (names of moorings used and distance covered in each test are indicated in the header). The last two rows show correlations at frequencies lower and higher than 4 months. All correlations in this Table have a p-value <0.01, as computed using the effective number of degrees of freedom (Emery and Thomson, 2001).

	test 1 22 km F3, F4	**test 2** 45 km F3 to F5	**test 3** 86 km F3 to F7	**test 4** 11 km M1_1, M1_2	**test 5** 65 km M1_1 to M1_3
Correlation	0.53	0.63	0.55	0.60	0.37
RMSD (cm s^{-1})	5.0	3.2	2.5	4.1	2.2
Correlation 4 months low-pass	0.57	0.66	0.64	0.59	0.39
Correlation 4 months high-pass	0.41	0.46	0.12	0.60	0.22

Appen et al., 2016; Pnyushkov et al., 2015). Furthermore, the time variability of the mesoscale processes is smoothed out in the altimetry dataset due to the 50 km decorrelation scale applied through the interpolation. This is reflected in the v_n standard deviation, which is about four to five times smaller than that of v_{ni} at most moorings.

Tests 1 to 5 show the scales over which spatial averaging improved the comparison (Table 7). In the Fram Strait, averaging over moorings F3 to F5 (test 2) yielded a correlation higher than that using data only from the F3 mooring (Tables 6 and 7). Results from tests 1 and 3 yielded correlations comparable to that from F3. All three tests reduce the RMSD by about 2-3 cm with respect to that at F3. At the Laptev Sea continental slope, neither test 4 nor test 5 improved the correlation with respect to the comparison at the M1_1 mooring. Both tests though reduce the RMSD with respect to the one at M1_1 (2-4 cm lower).

With regards to temporally filtering of the time series in tests 1 to 5, we find that seasonal to interannual frequencies explain most of the variability both in v_n and in v_{ni}. They constitute about 80% of the total variability in the Fram Strait, and about 90% at the Laptev Sea continental slope. In this frequency band v_n and in v_{ni} correlate better or equally than without filtering (Table 7), whereas in the intra-seasonal frequency band the correlation worsen.

The fact that seasonal to interannual frequencies explain a high percentage of the total variability can be attributed to the dominant seasonal oscillations. These are visible for instance in Fig. 9a and Fig. 10a, which show the low-pass filtered v_n and v_{ni} from tests 2 and 4. Seasonal cycles of v_n and v_{ni} are in phase, with peaks occurring in winter, and troughs in early summer; both in the Fram Strait and at the Laptev Sea continental slope. Furthermore, v_n and v_{ni} show similarities in the interannual variability. For instance, in the Fram Strait both datasets feature a double peaked seasonal oscillation in some years (e.g. winters 2013-2014, 2014-2015, 2017-2018). At the Laptev Sea continental slope the seasonal cycle amplitude decreases in both datasets between 2016 and 2018 .

https://doi.org/10.5194/essd-2021-170
Preprint. Discussion started: 25 May 2021

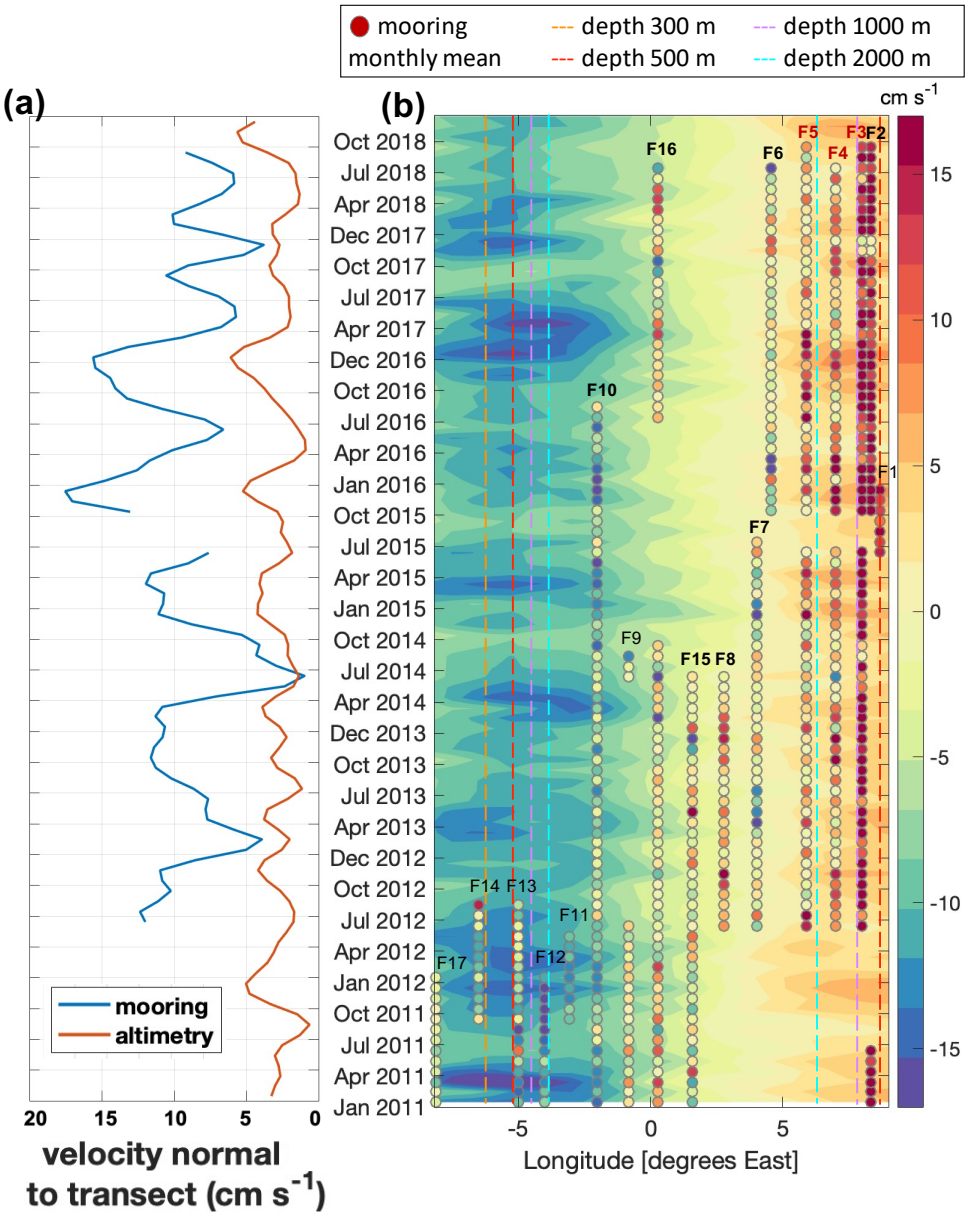

Figure 9. The altimetry-derived geostrophic velocity is shown against the in-situ surface velocity at the moorings transects in the Fram Strait (see Fig. 1). The component of the velocity normal to the transect is evaluated, and positive values represent northward velocity. (a) Scatterplot of all monthly values of satellite-derived velocities against in-situ velocities. (b) longitudinal average of altimetry and in-situ velocity across moorings indicated with red letters in panel (c) (corresponding to test 2, see Sect. 5.2.2); both time series have been filtered with a 4-months low pass filter. (c) Hovmöller diagram representing the monthly temporal evolution of the altimetry-derived cross-transect geostrophic velocity. The circles represent monthly mean values of in-situ cross-transect velocity measured at 75 m water depth. Dashed vertical lines represent the positions, along the transect, of the bottom topography isolines at 300 m (orange), 500 m (red), 1000 m (violet) and 2000 m (cyan) depth. On the top part of the diagram we indicated the position of each mooring; moorings with bold letters have more than 24 months available.

https://doi.org/10.5194/essd-2021-170
Preprint. Discussion started: 25 May 2021

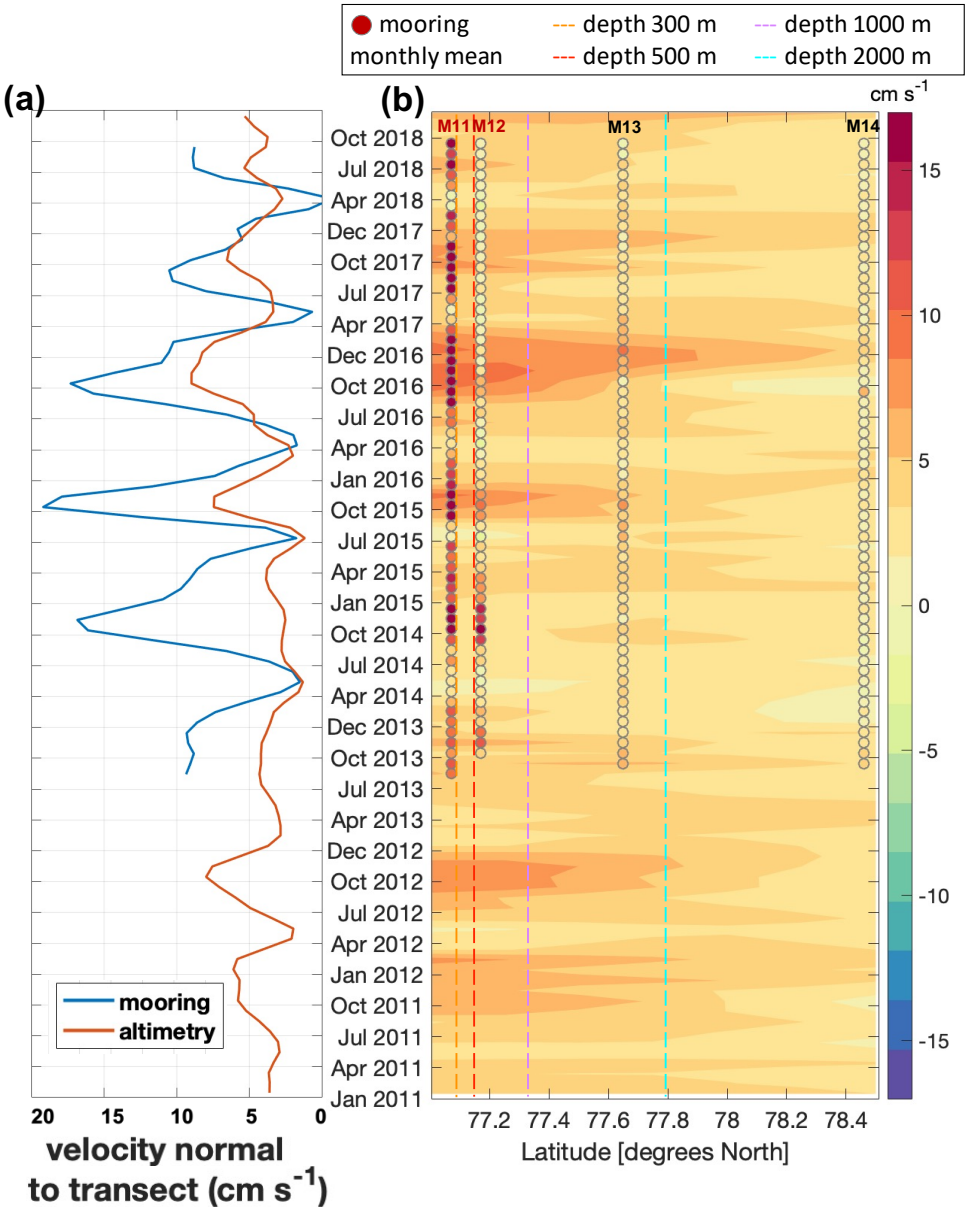

Figure 10. As in Fig. 9, for velocities at the Laptev Sea continental slope (see Fig. 1). The component of the velocity normal to the transect is positive eastward. in-situ velocity is averaged vertically between 50 m and 8 m depth (except at M1_1, averaged between 50 m and 30 m). The time series in panel (b) correspond to test 4 (see text).

https://doi.org/10.5194/essd-2021-170
Preprint. Discussion started: 25 May 2021


Open Access Earth System Science Data Discussions

5.3 Seasonal cycle

In the following text we give an overview regarding the seasonal cycle observed in η' and (u_g, v_g), highlighting which are the regions where it explains a high fraction of the total variability.

5.3.1 Sea surface height anomaly

The amplitude A and the phase α of the η' seasonal cycle (i.e., month when the maximum occurs) are shown in Fig. 11. Regions where the seasonal cycle explains less than 20% of the total variability are blanked in Fig. 11b. The seasonal cycle explains more than 20% of the total variability in shallow shelf regions (with a peak of 60% in the Barents Sea) and in few deep regions like the southwestern Canada Basin, the Baffin Bay and the Nordic Seas. Here, the amplitude ranges between 3 cm and 8 cm (Fig. 11a). Instead, seasonal variability seems to play little role in the Arctic Deep Basins, where its amplitude is <1 cm. η'_{seas} is maximum in early winter across the Arctic Ocean, even though not uniformly. η'_{seas} peaks earliest (September-October) in the Nordic Seas, the Chukchi Shelf and the Baffin Bay (Fig. 11b). A maximum around November-December is found further inside the Arctic, in the Barents and western Kara Seas, in the Laptev Sea and East Siberian Sea and in the southwestern Canada Basin. The maxima in the eastern Kara Sea (January) and the northeast Greenland Shelf (January-February) are later in the winter.

In Fig. 11c we also display the observed η' monthly climatology in selected regions, computed as the January to December monthly averages over the years 2011-2018. We see that the harmonic fit is a good approximation of the climatology in most of these regions, with few exceptions. For instance, in the Canada Basin, the Baffin Bay and the northeastern Greenland Shelf the climatology exhibits a secondary peak in April.

5.3.2 Geostrophic velocity

Fig. 12 shows the winter (January to March) and summer (June to August) (u_g, v_g) fields, averaged over the period 2011-2018. Seasonal speed anomalies are most pronounced south of 80ºN, namely along the shelf edges, in some coastal regions, in the southern Canada Basin and in the Barents Sea. The strongest variation in current speed between summer and winter is about 3 cm s^{-1}. The time of seasonal maximum of some of the main Arctic currents is shown in Table 8. From the comparison between summer and winter current anomalies we observe a basin wide, coherent seasonal acceleration of the Arctic slope currents in winter and a deceleration in summer. The speed of these slope currents peaks between September and April. Namely, currents along the Nansen Basin shelf break, between the Fram Strait and the Lomonosov Ridge, peak in early winter (September to December); currents along the eastern shelf break of the Nordic Seas, in the Barents Sea and in the Baffin Bay peak in mid winter (November to February); the East Greenland Current peaks in late winter (February to April). Seasonality is also recognisable in some currents not along the continental slopes. For instance, currents along the Siberian coasts, in the Kara Sea (maximum between September and December) and in the East Siberian Sea (maximum between March and May). Another example are the southern and western branches of the Beaufort Gyre, where currents peak respectively in November-January and March-May.

https://doi.org/10.5194/essd-2021-170
Preprint. Discussion started: 25 May 2021

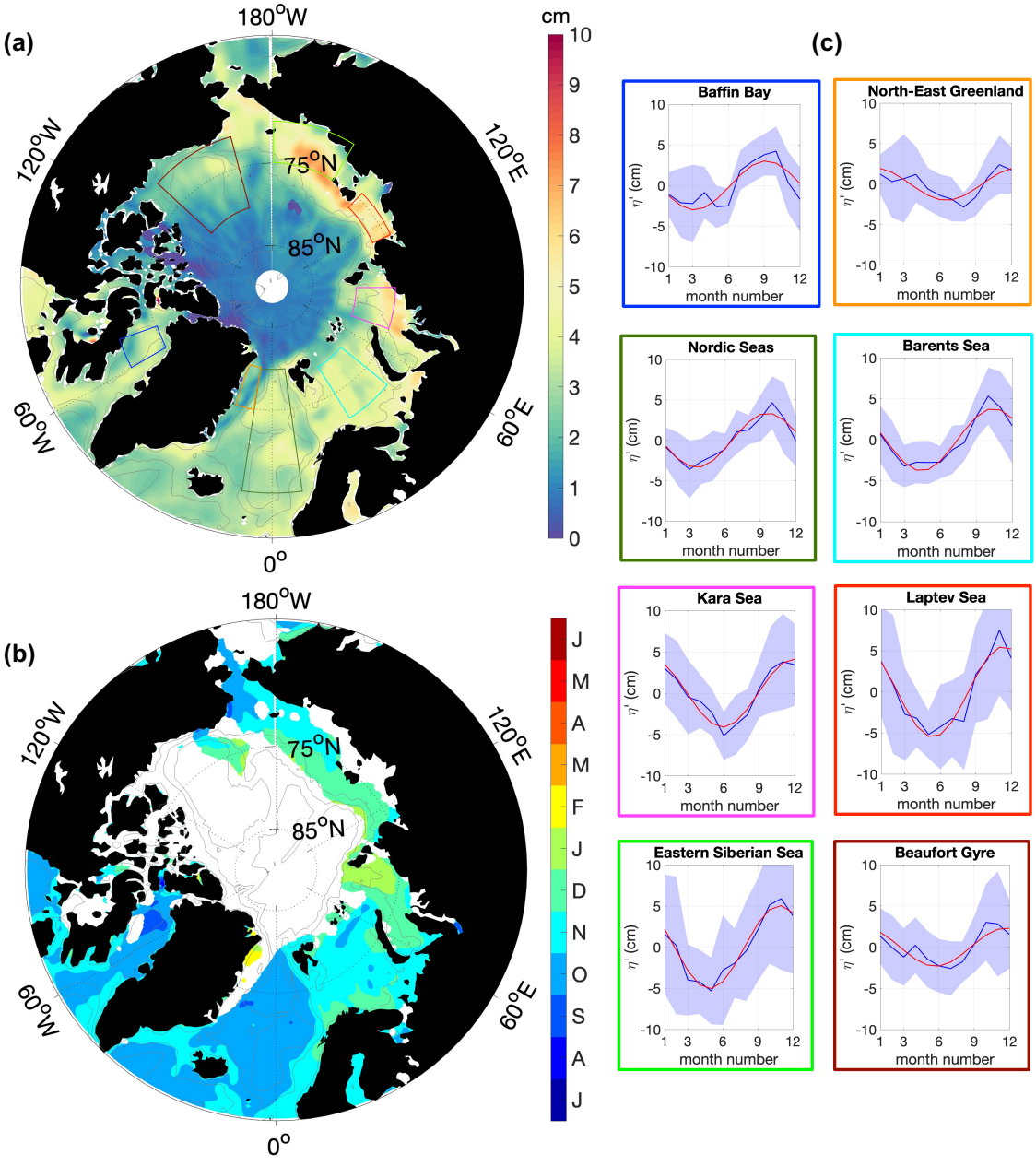

Figure 11. (a) Amplitude and (b) phase of the η' annual harmonic oscillation between 2011 an 2018. Blanked areas in (b) are those areas where the seasonal cycle explains less than 20% of the total variance. Panels in (c) are the η' monthly climatology (blue line, with standard deviation as shading) and the η'_{seas} (red line) averaged over the areas marked in the map with the corresponding color. Bathymetry contours are drawn at 100 m, 1000 m and 2500 m depth.

https://doi.org/10.5194/essd-2021-170
Preprint. Discussion started: 25 May 2021

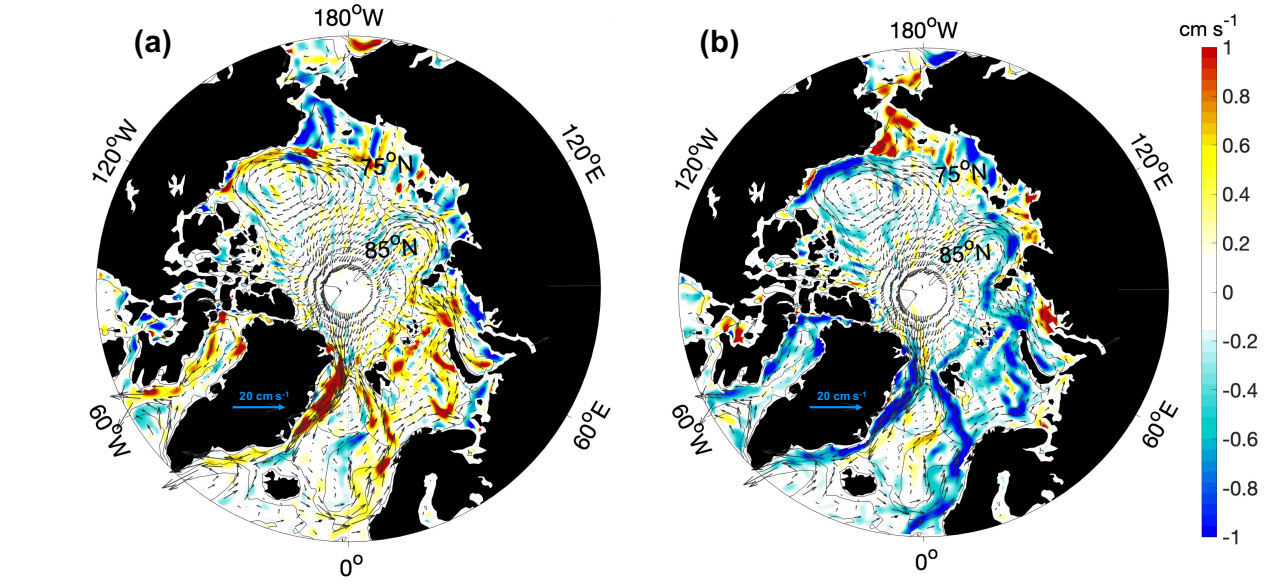

Figure 12. Averages of the the (u_g, v_g) fields over the (a) winter months January-February-March and the (b) summer months June-July-August. Bathymetry contours are drawn at 100 m, 1000 m and 2500 m depth. Arrows and colours are to be interpreted as described for Fig. 6b.

6 Discussion

The dataset presented in this paper provides 8 years of monthly maps of altimetry-derived sea surface height anomaly η' up to 88° N. In addition, we also provide the associated geostrophic velocity (u_g, v_g), which was not available before north of 82° N. We performed an Arctic wide comparison against an independent altimetry product. Results from this comparison indicate isolated areas where the correlation between data sets is low. Thus, here we discuss whether this is related to the methods used. We also carried out a comparison to in-situ data of both sea surface height and surface velocity in three seasonally ice-covered regions. We discuss these results in terms of the spatial and temporal resolution of our altimetry-derived velocity and the underlying dynamic regimes. Finally we put our findings on the seasonal cycle of sea surface height and geostrophic flow in the context of previous literature.

6.1 Impact of methodology

The comparison with the CPOM DOT (Sect. 5.2.1) yielded a correlation higher than 0.7 over most of the domain, but lower in some regions, with non-negligible differences between the datasets there. What are the methodological steps that may generate differences between these two data sets?

Regional differences might occur due to different data density, which results from distinct algorithms used for the processing of waveforms. In our comparison the correlation is low in some areas of the ice-covered Arctic. In ice-covered regions the

https://doi.org/10.5194/essd-2021-170
Preprint. Discussion started: 25 May 2021

Open Access Earth System Science Data Discussions

Table 8. Time of seasonal maximum occurrence in the currents of the Arctic Ocean in the results of this study. The acronym of currents correspond to those indicated in Fig. 1 and slope currents are marked in bold. The third column indicate studies which find seasonality in agreement with our results.

Current	Time of seasonal maximum	Other studies
WSC (and NwASC)	November to February	Beszczynska-Möller et al. (2012); von Appen et al. (2016)
BSB	November to February	Schauer et al. (2002)
VSC	September to December	Janout et al. (2015)
ACBC	October to January (western Nansen Basin) September to December (Laptev Sea continental Slope)	Pérez Hernández et al. (2019) Baumann et al. (2018)
BG	November to January (southern branch) March to May (western branch)	Proshutinsky et al. (2009); Armitage et al. (2017) Min et al. (2019)
SCC	March to May	Weingartner et al. (1999); Osadchiev et al. (2020)
BIC	November to February	Tang et al. (2004) (peak in June-August)
EGC	February to April	Bacon et al. (2014); Le Bras et al. (2018); de Steur et al. (2018)

detection of leads is based on surface classification techniques. These differ substantially between studies, and are to date a source of uncertainty (Dettmering et al., 2018). For instance, more observations are discarded the more conservative a technique is. This yields lower uncertainty, but also lower data density in the central and western Arctic, where the most compact multi year ice is located and lead density is low (Willmes and Heinemann, 2016). Thus, differences in the ice-covered regions are expected, given that Cryosat-2 observations are not classified in the AWI and CPOM DOT datasets using the same parameters and thresholds (Ricker et al., 2014; Armitage et al., 2016).

Generating data over the marginal ice zone still represents a challenge to overcome. This is because neither ocean-type retrackers nor ice-type retrackers are suitable to process altimetry waveforms there. Thus the coverage of these areas depends on the integration of data from ice-free and ice-covered areas, e.g. via interpolation, which is thus less constrained by actual data. It is perhaps not surprising then, that the correlation lower than 0.7 resulting from our comparison corresponds to open ocean areas of the central Arctic, where large patches of low ice concentration form at the end of summer. While we are aware that in our case neither the AWI nor the RADS dataset provide data in the marginal ice zone, not enough information on the CPOM DOT data coverage is available from Armitage et al. (2016).

We also found that sub-monthly η' variability in the Arctic can yield substantial noise in the monthly maps, especially on the shelves (Sect. 4.3.1). To reduce this noise we took two steps: first, we substituted the IB with the DAC correction in ice-

https://doi.org/10.5194/essd-2021-170
Preprint. Discussion started: 25 May 2021

covered regions (Sect. 4.2.2); second, we performed the interpolation on weekly data input rather than monthly (Sect. 4.3.1). This approach yielded improvements relative the CPOM DOT dataset. For example, in the East Siberian Sea and the Chukchi Sea regions, where the sub-monthly variability is strongest, our monthly η' fields have average spatial standard deviation of 6 cm for the period 2011-2014. This significantly lower than the corresponding value of 11 cm for the same region and period in the CPOM DOT. This might be attributable to larger unresolved sub-monthly variability in the CPOM DOT.

6.2 Comparison between satellite altimetry retrievals and in-situ data

Independent in-situ sea surface height from mooring data were used to assess our altimetry product in two separate regions of the central Arctic, i.e. the Fram Strait and the Nansen Basin. Results showed that altimetry and in situ data yield roughly consistent patterns, e.g. a clear seasonal signal in the Fram Strait and enhanced monthly variability in the Nansen Basin. Thus, both datasets consistently suggest that the sea surface height variability has different dominant time scales in the two basins. Correlations for our open ocean comparison between altimetry and mooring observations were low relative to previous studies which compared altimetry and near-shore tide gauge measurements (Volkov and Pujol, 2012; Armitage et al., 2016; Rose et al., 2019). This can be expected given that tide gauges measure sea surface height, directly comparable to altimetry. Also, we expect sea surface height variability near the coast to show larger amplitudes than in the open ocean (see Fig. 11). At the same time, uncertainties arise when estimating sea surface height from mooring data, as a result of limited vertical resolution of density observation. Nevertheless, the amplitude of RMSD between altimetry and open ocean mooring observations were consistent with other studies comparing altimetry to in-situ observations. RMSD values in the range of 2 to 12 cm has been found both from the comparison with tide gauges across the Arctic (Volkov and Pujol, 2012; Armitage et al., 2016; Rose et al., 2019) and with steric height measured in the Arctic Deep Basins (Kwok and Morison, 2011).

One comparison of altimetry-derived currents with moored currents velocity was done previous to this work by Armitage et al. (2017). Despite this comparison was performed in a region other than those considered here, results are consistent with those of this work. Their correlation to ADCP measurements in the interior of the Beaufort Sea, lower or equal to 0.54, are in line with our findings at most mooring sites except for mooring M1_1, which shows higher correlation (0.77). RMSD of 1-2 cm s^{-1} over currents of 1-6 cm s^{-1} also agrees well with the RMSD that we find in the interior of the Eurasian Basin (1.3-1.9 cm s^{-1}).

6.3 Temporal and spatial resolution of altimetry-derived currents

The large spatial extent of mooring velocity measurements and their long deployment period allowed us to examine the correlation of altimetry and in-situ velocity over both different dynamic regimes and spatio-temporal scales.

We found that correlation was higher in regions where the flow variability is dominated by steady currents (i.e. boundary currents) and lower where it is dominated by nonstationary eddy activity. In the Fram Strait, altimetry and in-situ data had the highest correlation on the shore and continental slope east of 5°E, within the West Spitsbergen Current, with maximum correlation in the core non-eddying part of the current (mooring F3, Beszczynska-Möller et al. (2012)). In the Laptev Sea the correlation was highest at mooring M1_1, close to the shelf break, where the the Arctic Circumpolar Boundary Current

https://doi.org/10.5194/essd-2021-170
Preprint. Discussion started: 25 May 2021

is strongest (Aksenov et al., 2011; Baumann et al., 2018). On the contrary, in both regions the correlation broke down where mean currents are slow and the mesoscale activity is enhanced. Namely, correlation was low and non significant at moorings in the central Fram Strait, where the surface circulation is dominated by westward eddies propagation (von Appen et al., 2016; Hattermann et al., 2016). Similarly, correlation was low in the offshore part of the Laptev Sea continental slope, where current speed is low and eddy activity increases (Pnyushkov et al., 2015, 2018; Baumann et al., 2018). The correlation varies with the dynamic regime due to the different sampling of mesoscale activity by moorings and by altimetry. Mesoscale features are not resolved in our monthly altimetry fields because of the 50 km smoothing scale used in the interpolation. This is equivalent to about ten times the local first baroclinic Rossby radius (Nurser and Bacon, 2014; von Appen et al., 2016; Pnyushkov et al., 2015), which roughly sets the horizontal scale of mesoscale eddies.

In-situ surface velocities were used thus to evaluate the effective spatial and temporal resolution of altimetry-derived currents. In the region of the West Spitsbergen Current, the correlation was higher when averaging horizontally the in-situ observations over 50 km relative to 20 km. This indicates that the boundary current variability as observed by our altimetry-derived velocity agree most closely with the in-situ observed variability when both are averaged across at least 50 km. Slightly lower correlation was shown when averaging data further into the central Fram Strait (see test 3 in Table 7), where we entered a different dynamic regime. Eddies are there a source of variability at intra-seasonal time scales, which is not resolved by altimetry and which biases the large scale average velocity from moorings. The considerations above suggest that our monthly geostrophic velocities can resolve seasonal to interannual variability of boundary currents wider than about 50 km. Mesoscale intra-seasonal variability is instead not resolved.

6.4 Seasonality

The sea surface height seasonal cycle is driven by changes in its steric component (due to sea ice melting and refreezing, solar insolation) and mass component (due to water accumulation or release, precipitation, evaporation, river runoff). Previous studies identified the seasonal cycle as the dominant component of the sea surface height variability in the Arctic (e.g., Volkov et al., 2013; Armitage et al., 2016; Müller et al., 2019). Our results confirm these findings, showing that this variability explains a fraction higher than 20% of the total variability in large areas of the Arctic, including the Arctic Shelves, the Nordic Seas and part of the Canada Basin. Additionally we found that seasonal to interannual variability explains more than 80% of the geostrophic velocity variability within boundary currents in the Fram Strait and at the Laptev Sea continental slope.

Large scale features emerge in the seasonal cycle of η' and (u_g, v_g). For instance, η' has over most of the Arctic seasonal maximum in the winter months between October and January. This is in agreement with previous studies of both steric height and ocean mass seasonality from in-situ data. From hydrographic profiles the steric height was found to peak between September and November in the Greenland and Norwegian Seas (Siegismund et al., 2007), in the central Barents Sea (Volkov et al., 2013) and in the Canada Basin (Proshutinsky et al., 2009). From bottom pressure records, Peralta-Ferriz et al. (2011) found winter-enhanced basin-wide ocean mass oscillations. This suggests that both density and mass changes favour the rise of sea surface height during winter in the Arctic. Furthermore, we found that the amplitude of the seasonal cycle of η', as well as the fraction of variability explained, are higher over the shelf regions than in deep ocean regions of the Arctic interior. This

https://doi.org/10.5194/essd-2021-170
Preprint. Discussion started: 25 May 2021

decoupling of shallow and deep region, as well as the Arctic-wide occurrence of the winter maximum, agree well with the two first Empirical Orthogonal Functions of sea surface height derived by Bulczak et al. (2015) and Armitage et al. (2016): a basin-wide oscillation and an anti-phase oscillation between shelf regions and deep basins. Lastly, geostrophic currents consistently strengthen along the continental slopes in winter and weaken in summer. The strengthening of boundary currents in winter was documented for several regions by previous studies based on in-situ data, satellite data and model output (Table 8).

Our dataset is thus able to describe the seasonality of sea surface height and geostrophic currents across the Arctic consistently with previous studies.

7 Conclusions

With this work we aim to support and contribute to basin scale observational studies of the Arctic Ocean circulation by providing a new gridded product of satellite-derived sea surface height anomaly (η') and geostrophic velocity (u_g, v_g). In this paper we present Arctic-wide monthly maps of η' and (u_g, v_g), spanning the years 2011 to 2018, covering both the ice-free and ice-covered parts of the ocean. We believe that this well documented and validated Arctic-wide dataset will be of help to the scientific community to further understand the Arctic Ocean surface circulation and sea surface height variability down to 50 km scale at seasonal to interannual time scales.

In our description and discussion of processing methods we find that residual sub-monthly variability in the Arctic Ocean is a source of noise for the η' monthly maps. Therefore, we average four weekly maps of interpolated data. Further, the integration of altimetry data over ice-free and ice-covered regions raises limitations in terms of data coverage between these two regions. Isolated differences in the comparison with the CPOM DOT are also attributable to the correction of sub-monthly variability and the data coverage in ice-covered regions, even though there is overall good agreement.

The comparison to in-situ sea surface height and near-surface velocity shows that the agreement varies between regions depending on the nature and scales of the variability. Geostrophic currents and in situ velocity have the highest correlation in regions where a stable flow (e.g. boundary currents) dominates the mesoscale eddy activity. There, the correlation is improved by spatially averaging in-situ data over cross-flow distances of at least 50 km and by filtering out intra-seasonal variability.

Overall, the comparison with in-situ data yields correlation and RMSD consistent with previous studies. The average correlation of η' with the sum of steric height and bottom pressure equivalent height is 0.41 and the average RMSD 4.1 cm. The correlation between (u_g, v_g) and near-surface moored velocity is highest at mooring sites within boundary currents both in the Fram Strait (0.53) and at the Laptev Sea continental slope (0.77). The average RMSD between velocities is 6.5 cm s^{-1} in the Fram Strait and 3.4 cm s^{-1} at the Laptev Sea continental slope.

Large scale patterns emerge from our preliminary analysis of the seasonal cycle of η' and (u_g, v_g). The η' shows a basin wide, coherent seasonal cycle, with maximum between October and January, and higher amplitude on the shelves. The (u_g, v_g) features intensification of the Arctic slope currents in winter and weakening in summer. These characteristics are in agreement with several regional studies of the Arctic Ocean sea surface height and boundary currents.

https://doi.org/10.5194/essd-2021-170
Preprint. Discussion started: 25 May 2021

Further uses of the sea surface height data product are the analysis of large-scale variability in upper ocean salinity and freshwater inventories.

https://doi.org/10.5194/essd-2021-170
Preprint. Discussion started: 25 May 2021


Open Access Earth System Science Data Discussions

8 Data availability

The final monthly maps of sea surface height anomaly and geostrophic velocity (2011-2018) can be downloaded from PANGAEA at [data under review]. These files include as auxiliary fields the sea surface height relative error and the DTU17MDT mean dynamic topography. The time series of steric height and bottom pressure equivalent height at moorings FS_S, AC and M1_4p6 as processed in this work are available from PANGAEA at [data under review].

The along-track sea surface height anomaly data used in this study are freely available online: open ocean data can be downloaded from the online Radar Altimetry Database System (RADS, http://rads.tudelft.nl/rads/rads.shtml); data from ice-covered regions can be obtained from the Meereisportal of the Alfred Wegener Institute (https://www.meereisportal.de). The CPOM DOT dataset can be accessed at http://www.cpom.ucl.ac.uk/dynamic_topography/. The in-situ velocity data from the Fram Strait can be downloaded from PANGAEA at https://doi.pangaea.de/10.1594/PANGAEA.900883 and https://doi.pangaea.de/10.1594/PANGAEA.904565 (von Appen et al., 2019; von Appen, 2019). The in-situ velocity data from the Laptev Sea continental slope can be downloaded from the NFS Arctic Data Center at https://arcticdata.io/catalog/view/doi:10.18739/A28G8FJ3H and https://arcticdata.io/catalog/view/doi:10.18739/A2HT2GB80 (Polyakov, 2016, 2019).

https://doi.org/10.5194/essd-2021-170
Preprint. Discussion started: 25 May 2021


Open Access Earth System Science Data Discussions

Appendix A: Dynamic Atmospheric Correction

The DAC corrects the local and the dynamic ocean response (waves) to pressure and wind changes and is derived from the sea surface height output of a barotropic model (Carrère and Lyard, 2003; Carrère et al., 2016). Up until the early 2000s, the effect of atmospheric pressure and winds on sea surface height had instead been corrected using an Inverse Barometer formula (IB, e.g., Ponte and Gaspar (1999); Carrère and Lyard (2003)). In the IB assumption, the sea surface height responds locally to changes in pressure, decreasing of approximately 1 cm for each increase in pressure of 1 mbar (atmospheric loading). However, it has been shown that the IB is not always a good approximation of the ocean response, especially on time scales shorter than 20 days (Carrère and Lyard, 2003).

Studies from the last two decades have shown that the deviation of ocean barotropic response from a simple IB is larger at higher latitudes (Stammer et al., 2000; Vinogradova et al., 2007; Quinn and Ponte, 2012). For instance, Quinn and Ponte (2012) found that the coherence between ocean mass variability (from GRACE satellite) and altimetric sea surface height variability after applying only IB correction, increases with latitude. In the Arctic, the effect of pressure and wind forcing is not only local but also travels eastwards over the shelves in the form of mass waves (Fukumori et al., 1998; Danielson et al., 2020; Fukumori et al., 2015; Peralta-Ferriz et al., 2011). However, to date there is no study showing the effect of this waves on sea surface height measured from altimetry.

Here we compare the reduction in altimetry standard deviation obtained by applying DAC with respect to IB in ice-covered regions of the Arctic Ocean. Fig. A1a shows the binned difference in standard deviation applying the two corrections, where positive values indicate better performance of DAC over IB. The DAC outperforms the IB in shallow shelf regions, and the two corrections perform equally well over the deep basins.

To understand which frequency bands have mostly contributed to this improvement, we take as an example the East Siberian Sea (yellow square indicated in Fig. A1a). We generated three time series of uncorrected η', η' corrected by IB and η' corrected by DAC, averaged with timestep of 1 day over the indicated region. For each year we analysed periods between November and July, which are the only months when data from leads are available. For each time series, we computed the standard deviation in frequency bands with periods T > 20 days, 5 days < T < 20 days, T < 5 days (Table A1). Results show that DAC reduced the uncorrected η' standard deviation by 50% at periods shorter than 20 days, in contrast to no reduction when applying a simple IB.

Furthermore, standard deviation at periods between 20 days and 5 days is larger then 60% the standard deviation at periods longer than 20 days, confirming how high frequency variability is relevant in the Arctic Ocean. The improvement of DAC with respect to IB over the shelves appears also in the η' monthly grids, where meridionally oriented patterns of η' are evidently reduced (two examples are given for the months of November 2014 and November 2017 in Fig. A2).

https://doi.org/10.5194/essd-2021-170
Preprint. Discussion started: 25 May 2021

Open Access Earth System Science Data Discussions

Table A1. Standard deviations of the three time series of along-track η', averaged over the East Siberian Sea box (Fig. A1), using uncorrected η', η' corrected by IB and η' corrected by DAC. For each year only ice-covered data are used, in the months November-July. Standard deviations are presented for the time series filtered in three different frequency bands.

standard deviation (cm) [uncorrected / IB / DAC]	T > 20 days	20 days > T > 5 days	T < 5 days
2011-2012	16.2 / 14.3 / 13.3	9.3 / 9.2 / 5.8	3.1 / 3.4 / 2.2
2012-2013	14.7 / 10.8 / 9.7	8.9 / 9.7 / 4.8	3.2 / 3.7 / 2.2
2013-2014	12.0 / 12.5 / 9.9	8.5 / 9.1 / 4.0	3.2 / 3.6 / 2.4
2014-2015	7.3 / 8.0 / 7.7	9.3 / 9.9 / 4.5	2.4 / 2.9 / 1.9
2015-2016	19.3 / 15.7 / 15.7	7.3 / 7.8 / 3.6	3.0 / 3.6 / 2.2
2016-2017	15.3 / 13.5 / 13.1	8.8 / 9.7 / 4.4	3.2 / 4.0 / 2.3
2017-2018	10.0 / 7.4 / 6.8	9.2 / 11.0 / 4.8	3.4 / 3.8 / 2.5

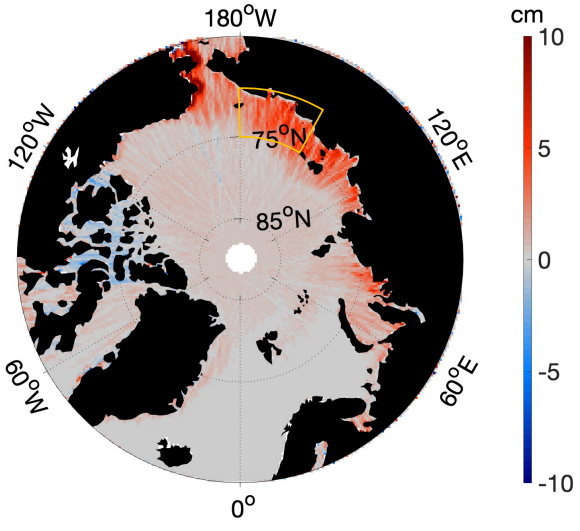

Figure A1. The along track improvement of DAC correction, with respect to IB, in removing η' high frequency variability. Colours indicate the difference between the standard deviation of along track η' corrected IB and corrected with DAC. The yellow square indicate the region of the East Siberian Sea where the frequency analysis was performed.

https://doi.org/10.5194/essd-2021-170
Preprint. Discussion started: 25 May 2021

Open Access Earth System Science Data Discussions

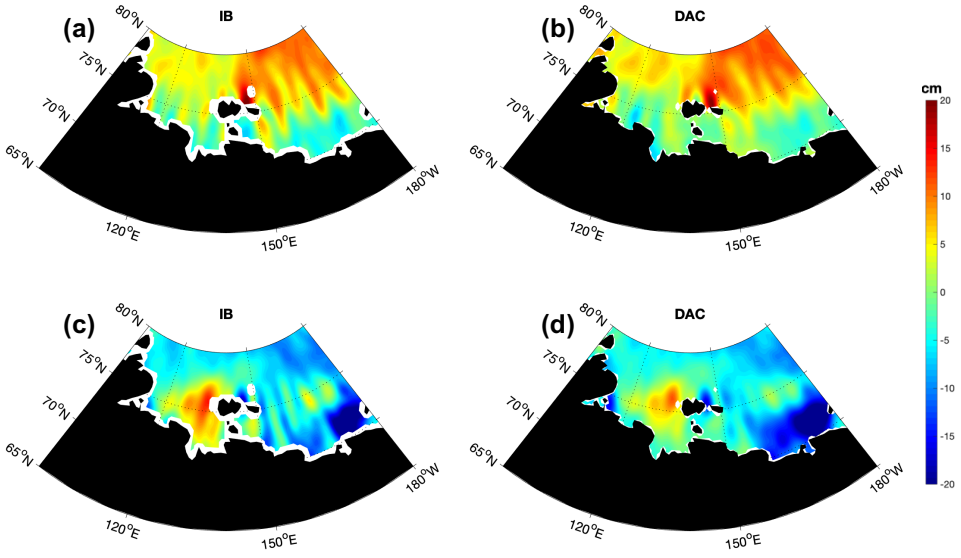

Figure A2. Effect of using correction DAC (panels (b) and (d)) instead of IB (panels (a) and (c)) on the monthly gridded η' fields (see Sect. 4.3). Two examples are shown for the months of November 2014 (panels (a) and (b)) and November 2017 (panels (c) and (d)).

Appendix B: Data-Interpolating Variational Analysis

The basic cost function applied in DIVA to derive the analysis field φ is expressed as a sum of terms which constrain the solution as follows (Eq. B1):

$$J(\varphi) = \sum_{i=1}^{N} \mu_i \cdot [d_i - \varphi(\mathbf{x}_i)] + \|\varphi\|^2 + J_c(\varphi) \tag{B1}$$

where d_i is the observation at the location $\mathbf{x}_i$, μ_i is the weight associated with each data point and $\|\cdot\|^2$ is a norm operator. The two fundamental properties minimized by this cost function (B1) are: 1) the deviation of the analysis field from observations (first term) and 2) abrupt changes in the analysis field (second term). Additional constraints $J_c(\varphi)$ can be applied.

The first term minimizes the misfits between data and analysis; weight associated to the misfits μ_i are directly proportional to the signal-to-noise ratio λ. λ is to be interpreted both as a measure of the observational error and as an indication how well data represent the final analysis field (e.g., instantaneous measurements are not a good representation of a long term mean). The second term generates a smooth analysis by applying the norm operator $\|\varphi\|^2$ over the grid domain Ω,:

$$\|\varphi\|^2 = \int_{\Omega} (\alpha_0 L^4 \varphi^2 + \alpha_1 L^2 \tilde{\nabla}\varphi \cdot \tilde{\nabla}\varphi + \tilde{\nabla}^2\varphi \cdot \tilde{\nabla}^2\varphi)\, d\Omega \tag{B2}$$

https://doi.org/10.5194/essd-2021-170
Preprint. Discussion started: 25 May 2021

where α_0 and α_1 are internal DIVA coefficients which set the relative importance of the derivatives (Troupin et al., 2012), $\tilde{\nabla}$ is the unitless gradient operator and L is the length used to scale the interpolation.

Additional constraints can be applied in DIVA, for instance the "advection constraint" which introduces anisotropic weighting of the data points:

$$J_c(\varphi) = \int_\Omega (\mathbf{v} \cdot \nabla\varphi)^2 \, d\Omega \tag{B3}$$

where $\mathbf{v} = a \cdot (u, v)$ is a vector field with a the scaling factor. Minimising $J_c(\varphi)$ constrains the analysis isolines along the vector field $\mathbf{v}$.

https://doi.org/10.5194/essd-2021-170
Preprint. Discussion started: 25 May 2021

Author contributions. FD processed the along-track data, performed the interpolation and the comparisons, wrote most of the text. RR provided the along-track observations in the ice-covered regions and supported the processing of those. BR contributed to the discussion and application of the interpolation method. TK supervised the work and advised on the comparison with in-situ data. All authors contributed to the discussion of the results and to the improvement of the manuscript.

Competing interests. The authors declare that they have no conflict of interest.

Acknowledgements. The processing of the CryoSat-2 sea surface height in ice-covered regions was funded by the German Ministry of Economics Affairs and Energy (grant: 50EE1008); data from 2011 to 2018 were obtained from https://www.meereisportal.de (grant:REKLIM-2013-04).

In-situ temperature and salinity data, ocean bottom pressure records and velocity data are available in the framework of the Helmholtz society strategic investment FRontiers in Arctic marine Monitoring (FRAM) as well as the Nansen and Amundsen Basins Observations System II program (NABOS-II, NSF grants AON-1203473, AON-1338948, and 1708427) and the joint Russian-German research project Changing Arctic Transpolar System (CATS). We are thankful to these projects for making publicly available quality controlled in-situ data. We thank expressly Vladimir Ivanov for leading the research expeditions of the CATS and NABOS-II project and making the data collection possible. The authors wish to thank Qiang Wang for sharing the output of the FESOM model.

The work of FD, TK and BR was part of the cooperative project REgional Atlantic Circulation and global changE (RACE) funded by the German Federal Ministry for Education and Research (BMBF), grant ID #03F0824E. The work of FD is a contribution to the "Helmholtz Climate Initiative REKLIM," a joint research project by the Helmholtz Association of German research centres (HGF). The work of BR further contributed to the project Advective Pathways of nutrients and key Ecological substances in the Arctic (APEAR) project (NE/R012865/1, NE/R012865/2, #03V01461), part of the Changing Arctic Ocean programme, jointly funded by the UKRI Natural Environment Research Council (NERC) and the German Federal Ministry of Education and Research (BMBF).

https://doi.org/10.5194/essd-2021-170
Preprint. Discussion started: 25 May 2021

References

Aksenov, Y., Ivanov, V. V., Nurser, A. J. G., Bacon, S., Polyakov, I. V., Coward, A. C., Naveira-Garabato, A. C., and Beszczynska-Moeller, A.: The Arctic Circumpolar Boundary Current, Journal of Geophysical Research, 116, 11, https://doi.org/10.1029/2010JC006637, 2011.

Alexandrov, V., Sandven, S., Wahlin, J., and Johannessen, O. M.: The relation between sea ice thickness and freeboard in the Arctic, The Cryosphere, 4, 373–380, https://doi.org/10.5194/tc-4-373-2010, 2010.

Andersen, O., Knudsen, P., and Stenseng, L.: The DTU13 MSS (Mean Sea Surface) and MDT (Mean Dynamic Topography) from 20 Years of Satellite Altimetry, in: IGFS 2014, pp. 111–121, Springer, Cham, Cham, https://doi.org/10.1007/1345_2015_182, 2015.

Armitage, T. W. K. and Davidson, M. W. J.: Using the Interferometric Capabilities of the ESA CryoSat-2 Mission to Improve the Accuracy of Sea Ice Freeboard Retrievals. , IEEE Transactions on Geoscience and Remote Sensing, 52, 529–536, https://doi.org/10.1109/TGRS.2013.2242082, 2014.

Armitage, T. W. K., Bacon, S., Ridout, A. L., Thomas, S. F., Aksenov, Y., and Wingham, D. J.: Arctic sea surface height variability and change from satellite radar altimetry and GRACE, 2003-2014, Journal of Geophysical Research: Oceans, 121, 4303–4322, https://doi.org/10.1002/2015JC011579, 2016.

Armitage, T. W. K., Bacon, S., Ridout, A. L., Petty, A. A., Wolbach, S., and Tsamados, M.: Arctic Ocean surface geostrophic circulation 2003–2014, The Cryosphere, 11, 1767–1780, https://doi.org/10.5194/tc-11-1767-2017, 2017.

Bacon, S., Marshall, A., Holliday, N. P., Aksenov, Y., and Dye, S. R.: Seasonal variability of the East Greenland Coastal Current, Journal of Geophysical Research: Oceans, 119, 3967–3987, https://doi.org/10.1002/2013JC009279, 2014.

Baumann, T. M., Polyakov, I. V., Pnyushkov, A. V., Rember, R., Ivanov, V. V., Alkire, M. B., Goszczko, I., and Carmack, E. C.: On the Seasonal Cycles Observed at the Continental Slope of the Eastern Eurasian Basin of the Arctic Ocean, Journal of Physical Oceanography, 48, 1451–1470, https://doi.org/10.1175/JPO-D-17-0163.1, 2018.

Beszczynska-Möller, A., Fahrbach, E., Schauer, U., and Hansen, E.: Variability in Atlantic water temperature and transport at the entrance to the Arctic Ocean, 1997–2010, ICES Journal of Marine Science, 69, 852–863, https://doi.org/10.1093/icesjms/fss056, 2012.

Birol, F., Fuller, N., Lyard, F., Cancet, M., Niño, F., Delebecque, C., Fleury, S., Toublanc, F., Melet, A., Saraceno, M., and Léger, F.: Coastal applications from nadir altimetry: Example of the X-TRACK regional products, Advances in Space Research, 59, 936–953, https://doi.org/10.1016/j.asr.2016.11.005, 2017.

Bouffard, J., Naeije, M., Banks, C. J., Calafat, F. M., Cipollini, P., Snaith, H. M., Webb, E., Hall, A., Mannan, R., Féménias, P., and Parrinello, T.: CryoSat ocean product quality status and future evolution, Advances in Space Research, 62, 1549–1563, https://doi.org/10.1016/j.asr.2017.11.043, 2017.

Bouzinac, C.: CryoSat Product Handbook, Tech. rep., European Space Agency, https://earth.esa.int/documents/10174/125272/CryoSat_Product_Handbook, 2012.

Bretherton, F. P., Davis, R. E., and Fandry, C. B.: A technique for objective analysis and design of oceanographic experiments applied to MODE-73, Deep Sea Research, 23, 559–582, https://doi.org/10.1016/0011-7471(76)90001-2, 1976.

Bruinsma, S. L., Förste, C., Abrikosov, O., Lemoine, J.-M., Marty, J.-C., Mulet, S., Rio, M. H., and Bonvalot, S.: ESA's satellite-only gravity field model via the direct approach based on all GOCE data, Geophysical Research Letters, 41, 7508–7514, https://doi.org/10.1002/2014GL062045, 2014.

https://doi.org/10.5194/essd-2021-170
Preprint. Discussion started: 25 May 2021

Bulczak, A. I., Bacon, S., Garabato, A. C. N., Ridout, A., Sonnewald, M. J. P., and Laxon, S. W.: Seasonal variability of sea surface height in the coastal waters and deep basins of the Nordic Seas, Geophysical Research Letters, 42, 113–120, https://doi.org/10.1002/(ISSN)1944-8007, 2015.

Carrère, L. and Lyard, F.: Modeling the barotropic response of the global ocean to atmospheric wind and pressure forcing - comparisons with observations, Geophysical Research Letters, 30, 405, https://doi.org/10.1029/2002GL016473, 2003.

Carrère, L., Faugère, Y., and Ablain, M.: Major improvement of altimetry sea level estimations using pressure-derived corrections based on ERA-Interim atmospheric reanalysis, Ocean Science, 12, 825–842, https://doi.org/10.5194/os-12-825-2016, 2016.

Cartwright, D. E. and Edden, A. C.: Corrected Tables of Tidal Harmonics, Geophysical Journal International, 33, 253–264., https://doi.org/https://doi.org/10.1111/j.1365-246X.1973.tb03420.x, 1973.

Danielson, S. L., Hennon, T. D., Hedstrom, K. S., Pnyushkov, A. V., Polyakov, I. V., Carmack, E. C., Filchuk, K., Janout, M., Makhotin, M., Williams, W. J., and Padman, L.: Oceanic Routing of Wind-Sourced Energy Along the Arctic Continental Shelves, Frontiers in Marine Science, 7, 815, https://doi.org/10.3389/fmars.2020.00509, 2020.

de Steur, L., Hansen, E., Gerdes, R., Karcher, M., Fahrbach, E., and Holfort, J.: Freshwater fluxes in the East Greenland Current: A decade of observations, Geophysical Research Letters, 36, 14 485, https://doi.org/10.1029/2009GL041278, https://agupubs.onlinelibrary.wiley.com/doi/full/10.1029/2009GL041278, 2009.

de Steur, L., Peralta-Ferriz, C., and Pavlova, O.: Freshwater Export in the East Greenland Current Freshens the North Atlantic, Geophysical Research Letters, 45, 13,359–13,366, https://doi.org/10.1029/2018GL080207, 2018.

Dettmering, D., Wynne, A., Müller, F. L., Passaro, M., and Seitz, F.: Lead Detection in Polar Oceans—A Comparison of Different Classification Methods for Cryosat-2 SAR Data, Remote Sensing, 10, 1190, https://doi.org/10.3390/rs10081190, 2018.

Emery, W. J. and Thomson, R. E.: Chapter 3 - Statistical Methods and Error Handling, in: Data Analysis Methods in Physical Oceanography, edited by Emery, W. J. and Thomson, R. E., pp. 193–304, Elsevier Science, Amsterdam, https://doi.org/https://doi.org/10.1016/B978-044450756-3/50004-6, 2001.

European Space Agency: Geophysical Corrections in Level 2 CryoSat Data Products, Tech. Rep. IDEAS-VEG-IPF-MEM-1288, European Space Agency, 2016.

Farrell, S. L., McAdoo, D. C., Laxon, S. W., Zwally, H. J., Yi, D., Ridout, A., and Giles, K. A.: Mean dynamic topography of the Arctic Ocean, Geophysical Research Letters, 39, 1–5, https://doi.org/10.1029/2011GL050052, 2012.

Fukumori, I., Raghunath, R., and Fu, L. L.: Nature of global large-scale sea level variability in relation to atmospheric forcing: A modeling study, Journal of Geophysical Research: Solid Earth, 103, 5493–5512, https://doi.org/10.1029/97JC02907, 1998.

Fukumori, I., Wang, O., Llovel, W., Fenty, I., and Forget, G.: A near-uniform fluctuation of ocean bottom pressure and sea level across the deep ocean basins of the Arctic Ocean and the Nordic Seas, Progress in Oceanography, 134, 152–172, https://doi.org/10.1016/j.pocean.2015.01.013, 2015.

Giles, K. A., Laxon, S. W., Ridout, A. L., Wingham, D. J., and Bacon, S.: Western Arctic Ocean freshwater storage increased by wind-driven spin-up of the Beaufort Gyre, Nature Geoscience, 5, 194–197, https://doi.org/10.1038/ngeo1379, 2012.

Gruber, T. and Willberg, M.: Signal and error assessment of GOCE-based high resolution gravity field models, Journal of Geodetic Science, 9, 71–86, https://doi.org/10.1515/jogs-2019-0008, 2019.

Guillot, A. and Prandi, P.: SLA Arctic, AVISO Users Newsletter, 17, 9–10, https://doi.org/10.24400/527896/a01-2020.001, 2020.

Haller, M., Brümmer, B., and Müller, G.: Atmosphere–ice forcing in the transpolar drift stream: results from the DAMOCLES ice-buoy campaigns 2007–2009, The Cryosphere, 8, 275–288, https://doi.org/10.5194/tc-8-275-2014, 2014.

https://doi.org/10.5194/essd-2021-170
Preprint. Discussion started: 25 May 2021

Hattermann, T., Isachsen, P. E., von Appen, W.-J., and Sundfjord, A.: Eddy-driven recirculation of Atlantic Water in Fram Strait, Geophysical Research Letters, 43, 3406–3414, https://doi.org/10.1002/(ISSN)1944-8007, 2016.

Hendricks, S. and Ricker, R.: Product User Guide & Algorithm Specification: AWI CryoSat-2 Sea Ice Thickness (version 2.2), 2019.

Jahn, A., Tremblay, L. B., Newton, R., Holland, M. M., Mysak, L. A., and Dmitrenko, I. A.: A tracer study of the Arctic Ocean's liquid freshwater export variability, Journal of Geophysical Research: Solid Earth, 115, 10 419, https://doi.org/10.1029/2009JC005873, 2010.

Janout, M. A., Aksenov, Y., Hölemann, J. A., Rabe, B., Schauer, U., Polyakov, I. V., Bacon, S., Coward, A. C., Karcher, M., Lenn, Y.-D., Kassens, H., and Timokhov, L.: Kara Sea freshwater transport through Vilkitsky Strait: Variability, forcing, and further pathways toward the western Arctic Ocean from a model and observations, Journal of Geophysical Research: Oceans, 120, 4925–4944, https://doi.org/10.1002/2014JC010635, 2015.

Kaur, S., Ehn, J. K., and Barber, D. G.: Pan-arctic winter drift speeds and changing patterns of sea ice motion: 1979–2015, Polar Record, 54, 303–311, https://doi.org/10.1017/S0032247418000566, 2018.

Knudsen, P., Andersen, O., and Maximenko, N.: A new ocean mean dynamic topography model, derived from a combination of gravity, altimetry and drifter velocity data, Advances in Space Research, https://doi.org/https://doi.org/10.1016/j.asr.2019.12.001, 2019.

Komjathy, A. and Born, G. H.: GPS-based ionospheric corrections for single frequency radar altimetry, Journal of Atmospheric and Solar-Terrestrial Physics, 61, 1197–1203, https://doi.org/10.1016/S1364-6826(99)00051-6, 1999.

Kwok, R. and Morison, J.: Dynamic topography of the ice-covered Arctic Ocean from ICESat, Geophysical Research Letters, 38, 1–6, https://doi.org/10.1029/2010GL046063, 2011.

Kwok, R. and Morison, J.: Sea surface height and dynamic topography of the ice-covered oceans from CryoSat-2: 2011-2014, Journal of Geophysical Research: Oceans, 121, 674–692, https://doi.org/10.1002/2015JC011357, 2016.

Kwok, R., Spreen, G., and Pang, S.: Arctic sea ice circulation and drift speed: Decadal trends and ocean currents, Journal of Geophysical Research: Oceans, 118, 2408–2425, https://doi.org/10.1002/jgrc.20191, 2013.

Laxon, S. W.: Sea ice altimeter processing scheme at the EODC, International Journal of Remote Sensing, 15, 915–924, https://doi.org/10.1080/01431169408954124, 1994.

Le Bras, I. A. A., Straneo, F., Holte, J., and Holliday, N. P.: Seasonality of Freshwater in the East Greenland Current System From 2014 to 2016, Journal of Geophysical Research: Oceans, 123, 8828–8848, https://doi.org/10.1029/2018JC014511, 2018.

Lyard, F., Lefevre, F., Letellier, T., and Francis, O.: Modelling the global ocean tides: modern insights from FES2004, Ocean Dynamics, 56, 394–415, https://doi.org/10.1007/s10236-006-0086-x, 2006.

Ma, B., Steele, M., and Lee, C. M.: Ekman circulation in the Arctic Ocean: Beyond the Beaufort Gyre, Journal of Geophysical Research: Oceans, 122, 3358–3374, https://doi.org/10.1002/2016JC012624, 2017.

McPhee, M. G.: Intensification of Geostrophic Currents in the Canada Basin, Arctic Ocean, Journal of Climate, 26, 3130–3138, https://doi.org/10.1175/JCLI-D-12-00289.1, 2012.

Min, L., Pickart, R. S., Spall, M. A., Weingartner, T. J., Lin, P., Moore, G. W. K., and Qi, Y.: Circulation of the Chukchi Sea shelfbreak and slope from moored timeseries, Progress in Oceanography, 172, 14–33, https://doi.org/10.1016/j.pocean.2019.01.002, 2019.

Mizobata, K., Watanabe, E., and Kimura, N.: Wintertime variability of the Beaufort gyre in the Arctic Ocean derived from CryoSat-2/SIRAL observations, Journal of Geophysical Research: Oceans, 121, 1685–1699, https://doi.org/10.1002/2015JC011218, 2016.

Mulet, S., Rio, M. H., Etienne, H., Artana, C., Cancet, M., Dibarboure, G., Feng, H., Husson, R., Picot, N., Provost, C., and Strub, P. T.: The new CNES-CLS18 Global Mean Dynamic Topography, Ocean Science, pp. 1–31, https://doi.org/10.5194/os-2020-117, 2021.

https://doi.org/10.5194/essd-2021-170
Preprint. Discussion started: 25 May 2021

Müller, F. L., Wekerle, C., Dettmering, D., Passaro, M., Bosch, W., and Seitz, F.: Dynamic Ocean Topography of the Greenland Sea: A comparison between satellite altimetry and ocean modeling, The Cryosphere, p. 611–626, https://doi.org/10.5194/tc-13-611-2019, 2019.

Nurser, A. J. G. and Bacon, S.: The Rossby radius in the Arctic Ocean, Ocean Science, 10, 967–975, https://doi.org/10.5194/os-10-967-2014, 2014.

Osadchiev, A. A., Pisareva, M. N., Spivak, E. A., Shchuka, S. A., and Semiletov, I. P.: Freshwater transport between the Kara, Laptev, and East-Siberian seas, Scientific Reports, 10, 1–14, https://doi.org/10.1038/s41598-020-70096-w, 2020.

Passaro, M., Cipollini, P., Vignudelli, S., Quartly, G. D., and Snaith, H. M.: ALES: A multi-mission adaptive subwaveform retracker for coastal and open ocean altimetry, Remote Sensing of Environment, 145, 173–189, https://doi.org/10.1016/j.rse.2014.02.008, 2014.

Pawlowicz, R., Beardsley, B., and Lentz, S.: Classical tidal harmonic analysis including error estimates in MATLAB using T_TIDE, Computers & Geosciences, 28, 929–937, https://doi.org/10.1016/S0098-3004(02)00013-4, 2002.

Peralta-Ferriz, C., Morison, J. H., Wallace, J. M., and Zhang, J.: A basin-coherent mode of sub-monthly variability in Arctic Ocean bottom pressure, Geophysical Research Letters, 38, https://doi.org/10.1029/2011GL048142, 2011.

Pérez Hernández, M. D., Pickart, R. S., Torres, D. J., Bahr, F., Sundfjord, A., Ingvaldsen, R., Renner, A. H. H., Möller, A. B., von Appen, W.-J., and Pavlov, V.: Structure, Transport, and Seasonality of the Atlantic Water Boundary Current North of Svalbard: Results From a Yearlong Mooring Array, Journal of Geophysical Research: Oceans, 124, 1679–1698, https://doi.org/10.1029/2018JC014759, 2019.

Pnyushkov, A. V., Polyakov, I. V., Ivanov, V. V., Aksenov, Y., Coward, A. C., Janout, M., and Rabe, B.: Structure and variability of the boundary current in the Eurasian Basin of the Arctic Ocean, Deep-Sea Research Part I, 101, 80–97, https://doi.org/10.1016/j.dsr.2015.03.001, 2015.

Pnyushkov, A. V., Polyakov, I. V., Padman, L., and Nguyen, A. T.: Structure and dynamics of mesoscale eddies over the Laptev Sea continental slope in the Arctic Ocean, Ocean Science, 14, 1329–1347, https://doi.org/10.5194/os-14-1329-2018, 2018.

Polyakov, I. V.: NABOS II - ADCP Water Current Data 2013 - 2015., Arctic Data Center, https://doi.org/doi:10.18739/A28G8FJ3H, 2016.

Polyakov, I. V.: Acoustic Dopper Current Profiler (ADCP) from moorings taken in the Eurasian and Makarov basins, Arctic Ocean, 2015-2018. , https://doi.org/doi:10.18739/A2HT2GB80, 2019.

Polyakov, I. V. and Rembert, R.: Conductivity, Temperature, Pressure (CTD) measurements from Sea Bird Electronics SBE37 instruments taken in the Eurasian and Makarov basins, Arctic Ocean, 2015-2018., Arctic Data Center, https://doi.org/doi:10.18739/A2NK3652R, 2019.

Ponte, R. M. and Gaspar, P.: Regional analysis of the inverted barometer effect over the global ocean using TOPEX/POSEIDON data and model results, Journal of Geophysical Research, 104, 15 587–15 601, https://doi.org/10.1029/1999JC900113, 1999.

Proshutinsky, A., Krishfield, R., Timmermans, M.-L., Toole, J., Carmack, E. C., McLaughlin, F., Williams, W. J., Zimmermann, S., Itoh, M., and Shimada, K.: Beaufort Gyre freshwater reservoir: State and variability from observations, Journal of Geophysical Research: Solid Earth, 114, 14 485, https://doi.org/10.1029/2008JC005104, 2009.

Proshutinsky, A. Y. and Johnson, M. A.: Two circulation regimes of the wind-driven Arctic Ocean, Journal of Geophysical Research: Solid Earth, 102, 12 493–12 514, https://doi.org/10.1029/97JC00738, https://agupubs.onlinelibrary.wiley.com/doi/full/10.1029/97JC00738, 1997.

Quinn, K. J. and Ponte, R. M.: High frequency barotropic ocean variability observed by GRACE and satellite altimetry, Geophysical Research Letters, 39, 1–5, https://doi.org/10.1029/2012GL051301, 2012.

Ricker, R., Hendricks, S., Helm, V., and Davidson, M.: Sensitivity of CryoSat-2 Arctic sea-ice freeboard and thickness on radar-waveform interpretation, The Cryosphere, 8, 1607–1622, https://doi.org/10.5194/tc-8-1607-2014, 2014.

https://doi.org/10.5194/essd-2021-170
Preprint. Discussion started: 25 May 2021

Ricker, R., Hendricks, S., and Beckers, J.: The Impact of Geophysical Corrections on Sea-Ice Freeboard Retrieved from Satellite Altimetry, Remote Sensing, 8, 1–15, https://doi.org/10.3390/rs8040317, 2016.

Rio, M. H., Guinehut, S., and Larnicol, G.: New CNES-CLS09 global mean dynamic topography computed from the combination of GRACE data, altimetry, and in situ measurements, Journal of Geophysical Research, 116, C11 001–25, https://doi.org/10.1029/2010JC006505, 2011.

Rose, S. K., Andersen, O. B., Passaro, M., Ludwigsen, C. A., and Schwatke, C.: Arctic Ocean Sea Level Record from the Complete Radar Altimetry Era: 1991–2018, Remote Sensing, 11, 1672, https://doi.org/10.3390/rs11141672, 2019.

Scharroo, R. and Lillibridge, J.: Non-Parametric Sea-State Bias Models and Their Relevance to Sea Level Change Studies, in: Envisat ERS Symposium, Salzburg, Austria, 2005.

Scharroo, R., Leuliette, E., Lillibridge, J., Byrne, D., Naeije, M., and Mitchum, G.: RADS: Consistent multi-mission products, in: Proc. of the Symposium on Years of Progress in Radar Altimetry, Venice, - September, Eur. Space Agency Spec. Publ., 2013.

Schauer, U., Loeng, H., Rudels, B., Ozhigin, V. K., and Dieck, W.: Atlantic Water flow through the Barents and Kara Seas , Deep-Sea Research Part I, https://doi.org/10.1016/S0967-0637(02)00125-5, 2002.

Siegismund, F., Johannessen, J., Drange, H., Mork, K. A., and Korablev, A.: Steric height variability in the Nordic Seas, Journal of Geophysical Research: Solid Earth, 112, 2733, https://doi.org/10.1029/2007JC004221, 2007.

Spreen, G., Kwok, R., and Menemenlis, D.: Trends in Arctic sea ice drift and role of wind forcing: 1992-2009, Geophysical Research Letters, 38, 1–6, https://doi.org/10.1029/2011GL048970, 2011.

Stammer, D., Wunsch, C., and Ponte, R. M.: De-aliasing of global high frequency barotropic motions in altimeter observations, Geophysical Research Letters, 27, 1175–1178, https://doi.org/10.1029/1999GL011263, 2000.

Tang, C., Ross, C., Yao, T., Petrie, B., DeTracey, B., and Dunlap, E.: The circulation, water masses and sea-ice of Baffin Bay, Progress in Oceanography, 63, 183–228, https://doi.org/10.1016/j.pocean.2004.09.005, 2004.

Troupin, C., Barth, A., Sirjacobs, D., Ouberdous, M., Brankart, J. M., Brasseur, P., Rixen, M., Alvera-Azcárate, A., Belounis, M., Capet, A., Lenartz, F., Toussaint, M. E., and Beckers, J. M.: Generation of analysis and consistent error fields using the Data Interpolating Variational Analysis (DIVA), Ocean Modelling, 52-53, 90–101, https://doi.org/10.1016/j.ocemod.2012.05.002, 2012.

Tsujino, H., Urakawa, S., Nakano, H., Small, R. J., Kim, W. M., Yeager, S. G., Danabasoglu, G., Suzuki, T., Bamber, J. L., Bentsen, M., Böning, C. W., Bozec, A., Chassignet, E. P., Curchitser, E., Boeira Dias, F., Durack, P. J., Griffies, S. M., Harada, Y., Ilicak, M., Josey, S. A., Kobayashi, C., Kobayashi, S., Komuro, Y., Large, W. G., Le Sommer, J., Marsland, S. J., Masina, S., Scheinert, M., Tomita, H., Valdivieso, M., and Yamazaki, D.: JRA-55 based surface dataset for driving ocean–sea-ice models (JRA55-do), Ocean Modelling, 130, 79–139, https://doi.org/https://doi.org/10.1016/j.ocemod.2018.07.002, 2018.

UNESCO: Algorithms for computation of fundamental properties of seawater, Tech. rep., https://darchive.mblwhoilibrary.org/bitstream/handle/1912/2470/059832eb.pdf, 1983.

Vinogradova, N. T., Ponte, R. M., and Stammer, D.: Relation between sea level and bottom pressure and the vertical dependence of oceanic variability, Geophysical Research Letters, 34, C03 010, https://doi.org/10.1029/2006GL028588, 2007.

Volkov, D. L. and Pujol, M. I.: Quality assessment of a satellite altimetry data product in the Nordic, Barents, and Kara seas, Journal of Geophysical Research, 117, 1–12, https://doi.org/10.1029/2011JC007557, 2012.

Volkov, D. L., Landerer, F. W., and Kirillov, S. A.: The genesis of sea level variability in the Barents Sea, Continental Shelf Research, 66, 92–104, https://doi.org/10.1016/j.csr.2013.07.007, 2013.

https://doi.org/10.5194/essd-2021-170
Preprint. Discussion started: 25 May 2021

von Appen, W.-J.: Physical oceanography and current meter data (including raw data) from FRAM moorings in the Fram Strait, 2016-2018, PANGAEA, https://doi.org/10.1594/PANGAEA.904565, 2019.

von Appen, W.-J., Schauer, U., Hattermann, T., and Beszczynska-Möller, A.: Seasonal Cycle of Mesoscale Instability of the West Spitsbergen Current, Journal of Physical Oceanography, 46, 1231–1254, https://doi.org/10.1175/JPO-D-15-0184.1, 2016.

von Appen, W.-J., Beszczynska-Möller, A., Schauer, U., and Fahrbach, E.: Physical oceanography and current meter data from moorings F1-F14 and F15/F16 in the Fram Strait, 1997-2016, PANGAEA, https://doi.org/10.1594/PANGAEA.900883, 2019.

Wahr, J. M.: Deformation induced by polar motion, Journal of Geophysical Research: Solid Earth, 90, 9363–9368, https://doi.org/10.1029/JB090iB11p09363, 1985.

Wang, Q., Wekerle, C., Danilov, S., Wang, X., and Jung, T.: A 4.5 km resolution Arctic Ocean simulation with the global multi-resolution model FESOM 1.4, Geoscientific Model Development, 11, 1229–1255, https://doi.org/10.5194/gmd-11-1229-2018, 2018.

Wang, Q., Wekerle, C., Danilov, S., Sidorenko, D., Koldunov, N., Sein, D., Rabe, B., and Jung, T.: Recent Sea Ice Decline Did Not Significantly Increase the Total Liquid Freshwater Content of the Arctic Ocean, Journal of Climate, 32, 15–32, https://doi.org/10.1175/JCLI-D-18-0237.1, 2019.

Wang, Q., Wekerle, C., Wang, X., Danilov, S., Koldunov, N., Sein, D., Sidorenko, D., von Appen, W.-J., and Jung, T.: Intensification of the Atlantic Water Supply to the Arctic Ocean Through Fram Strait Induced by Arctic Sea Ice Decline, Geophysical Research Letters, 47, 2016, https://doi.org/10.1029/2019GL086682, 2020.

Weingartner, T. J., Danielson, S., Sasaki, Y., Pavlov, V., and Kulakov, M.: The Siberian Coastal Current: A wind- and buoyancy-forced Arctic coastal current, Journal of Geophysical Research: Solid Earth, 104, 29 697–29 713, https://doi.org/10.1029/1999JC900161, 1999.

Willmes, S. and Heinemann, G.: Sea-Ice Wintertime Lead Frequencies and Regional Characteristics in the Arctic, 2003–2015, Remote Sensing, 8, 4, https://doi.org/10.3390/rs8010004, 2016.

Wingham, D. J., Francis, C. R., Baker, S., Bouzinac, C., Brockley, D., Cullen, R., de Chateau-Thierry, P., Laxon, S. W., Mallow, U., Mavrocordatos, C., Phalippou, L., Ratier, G., Rey, L., Rostan, F., Viau, P., and Wallis, D. W.: CryoSat: A mission to determine the fluctuations in Earth's land and marine ice fields , Advances in Space Research, 37, 841–871, https://doi.org/10.1016/j.asr.2005.07.027, 2006.